The Astrophysical Journal, 992:100 (26pp), 2025 October 10 https://doi.org/10.3847/1538-4357/adfa23

Final Moments. III. Explosion Properties and Progenitor Constraints of CSM-interacting Type II Supernovae

W. V. Jacobson-Galán[1,2,40], L. Dessart[3], K. W. Davis[4], K. A. Bostroem[5], C. D. Kilpatrick[6,7], R. Margutti[2,8], A. V. Filippenko[2], R. J. Foley[4], R. Chornock[2], G. Terreran[9], D. Hiramatsu[10,11], M. Newsome[9,12], E. Padilla Gonzalez[9,12], C. Pellegrino[13], D. A. Howell[9,12], J. P. Anderson[14,15], C. R. Angus[16,17], K. Auchettl[4,18], T. G. Brink[2], R. Cartier[19], D. A. Coulter[20], T. de Boer[21], M. R. Drout[22], N. Earl[23], K. Ertini[24,25], J. R. Farah[9,12], D. Farias[16], C. Gall[16], H. Gao[21], M. A. Gerlach[26], F. Guo[27], A. Haynie[28,29], G. Hosseinzadeh[30], A. L. Ibik[22], S. W. Jha[31], D. O. Jones[32], D. Langeroodi[16], N. LeBaron[2], E. A. Magnier[21], A. L. Piro[28], S. I. Raimundo[16,33], A. Rest[34,20], S. Rest[34], R. Michael Rich[35], C. Rojas-Bravo[4], H. Sears[31], K. Taggart[4], V. A. Villar[10], R. J. Wainscoat[21], X.-F. Wang[27], A. R. Wasserman[36,37], S. Yan[27], Y. Yang[2,27], J. Zhang[38,39], and W. Zheng[2]

[1] Department of Astronomy and Astrophysics, California Institute of Technology, Pasadena, CA 91125, USA; wynnjg@caltech.edu
[2] Department of Astronomy, University of California, Berkeley, CA 94720-3411, USA
[3] Institut d'Astrophysique de Paris, CNRS-Sorbonne Université, 98 bis boulevard Arago, F-75014 Paris, France
[4] Department of Astronomy and Astrophysics, University of California, Santa Cruz, CA 95064, USA
[5] Steward Observatory, University of Arizona, 933 North Cherry Avenue, Tucson, AZ 85721-0065, USA[41]
[6] Center for Interdisciplinary Exploration and Research in Astrophysics (CIERA), Northwestern University, Evanston, IL 60202, USA
[7] Department of Physics and Astronomy, Northwestern University, Evanston, IL 60208, USA
[8] Department of Physics, University of California, Berkeley, CA 94720-7300, USA
[9] Las Cumbres Observatory, 6740 Cortona Drive, Suite 102, Goleta, CA 93117, USA
[10] Center for Astrophysics | Harvard & Smithsonian, 60 Garden Street, Cambridge, MA 02138-1516, USA
[11] The NSF AI Institute for Artificial Intelligence and Fundamental Interactions, USA
[12] Department of Physics, University of California, Santa Barbara, Santa Barbara, CA 93111, USA
[13] Department of Astronomy, University of Virginia, Charlottesville, VA 22904, USA
[14] European Southern Observatory, Alonso de Córdova 3107, Casilla 19, Santiago, Chile
[15] Millennium Institute of Astrophysics MAS, Nuncio Monsenor Sotero Sanz 100, Oficina 104, Providencia, Santiago, Chile
[16] DARK, Niels Bohr Institute, University of Copenhagen, Jagtvej 128, 2200 Copenhagen, Denmark
[17] Astrophysics Research Centre, School of Mathematics and Physics, Queen's University Belfast, Belfast BT7 1NN, UK
[18] School of Physics, The University of Melbourne, VIC 3010, Australia
[19] Centro de Astronomía (CITEVA), Universidad de Antofagasta, Avenida Angamos 601, Antofagasta, Chile
[20] Space Telescope Science Institute, Baltimore, MD 21218, USA
[21] Institute for Astronomy, University of Hawaii, 2680 Woodlawn Drive, Honolulu, HI 96822, USA
[22] David A. Dunlap Department of Astronomy and Astrophysics, University of Toronto, 50 Saint George Street, Toronto, Ontario, M5S 3H4, Canada
[23] Department of Astronomy, University of Illinois at Urbana-Champaign, 1002 West Green Street, Urbana, IL 61801, USA
[24] Facultad de Ciencias Astronómicas y Geofísicas, Universidad Nacional de La Plata, Paseo del Bosque S/N, B1900FWA, La Plata, Argentina
[25] Instituto de Astrofisica de La Plata (IALP), CCT-CONICET-UNLP, Paseo del Bosque S/N, B1900FWA, La Plata, Argentina
[26] Department of Astrophysics, Pontificia Universidad Catolica de Chile, Santiago, Chile
[27] Department of Physics, Tsinghua University, Shuangqing Road, Beijing, People's Republic of China
[28] The Observatories of the Carnegie Institute for Science, 813 Santa Barbara Street, Pasadena, CA 91101, USA
[29] Department of Physics & Astronomy, University of Southern California, Los Angeles, CA 90089, USA
[30] Department of Astronomy & Astrophysics, University of California, San Diego, 9500 Gilman Drive, MC 0424, La Jolla, CA 92093-0424, USA
[31] Department of Physics and Astronomy, Rutgers, the State University of New Jersey, 136 Frelinghuysen Road, Piscataway, NJ 08854, USA
[32] Institute for Astronomy, University of Hawai'i, 640 N. A'ohoku Pl., Hilo, HI 96720, USA
[33] Department of Physics and Astronomy, University of Southampton, Highfield, Southampton SO17 1BJ, UK
[34] Department of Physics and Astronomy, The Johns Hopkins University, Baltimore, MD 21218, USA
[35] Department Physics and Astronomy, University of California, Los Angeles, CA 90095-1547, USA
[36] Department of Astronomy, University of Illinois at Urbana-Champaign, 1002 West Green Street, IL 61801, USA
[37] Center for Astrophysical Surveys, National Center for Supercomputing Applications, Urbana, IL 61801, USA
[38] Yunnan Observatories (YNAO), Chinese Academy of Sciences, Kunming 650216, People's Republic of China
[39] Key Laboratory for the Structure and Evolution of Celestial Objects, CAS, Kunming, 650216, People's Republic of China
Received 2025 May 7; revised 2025 August 4; accepted 2025 August 7; published 2025 October 8

Abstract

We present analysis of the plateau and late-time phase properties of a sample of 39 Type II supernovae (SNe II) that show narrow, transient, high-ionization emission lines (i.e., "IIn-like") in their early-time spectra from interaction with confined, dense circumstellar material (CSM). Originally presented by W. V. Jacobson-Galán et al., this sample also includes multicolor light curves and spectra extending to late-time phases of 35 SNe with

[40] NASA Hubble Fellow.
[41] LSST-DA Catalyst Fellow.

no evidence for IIn-like features at <2 days after first light. We measure photospheric phase light-curve properties for the distance-corrected sample and find that SNe II with IIn-like features have significantly higher luminosities and decline rates at +50 days than the comparison sample, which could be connected to inflated progenitor radii, lower ejecta mass, and/or persistent CSM interaction. However, we find no statistical evidence that the measured plateau durations and ^{56}Ni masses of SNe II with and without IIn-like features arise from different distributions. We estimate progenitor zero-age main-sequence (ZAMS) masses for all SNe with nebular spectroscopy through spectral model comparisons and find that most objects, both with and without IIn-like features, are consistent with progenitor masses $\leqslant 12.5\,M_{\odot}$. Combining progenitor ZAMS masses with CSM densities inferred from early-time spectra suggests multiple channels for enhanced mass loss in the final years before core collapse, such as a convection-driven chromosphere or binary interaction. Finally, we find spectroscopic evidence for ongoing ejecta-CSM interaction at radii $>10^{16}$ cm, consistent with substantial progenitor mass-loss rates of 10^{-4}–$10^{-5}\,M_{\odot}$ yr^{-1} ($v_w < 50$ km s^{-1}) in the final centuries to millennia before explosion.

Unified Astronomy Thesaurus concepts: Type II supernovae (1731); Core-collapse supernovae (304); Supernovae (1668); Red supergiant stars (1375)

1. Introduction

A fundamental goal in the study of Type II supernovae (SNe II) is to connect explosion properties to the evolution of red supergiant (RSG) stars in their final years before core collapse. After shock breakout and the rise to peak brightness, SNe II are powered by hydrogen recombination and the cooling of a shocked, expanding RSG envelope during their light-curve "plateau"—this phase being defined observationally by the plateau's duration, brightness, and slope (J. P. Anderson et al. 2014; N. E. Sanders et al. 2015; S. Valenti et al. 2016; L. Martinez et al. 2022a). Theoretically, variations in these observables map to differences in kinetic energy, progenitor radius, ejecta mass, and/or ^{56}Ni mass (D. Kasen et al. 2006; L. Dessart et al. 2013; D. Hiramatsu et al. 2021a). By calibrating to numerical simulations, scaling relations between these quantities have been constructed that relate SN II light-curve properties to regions of the progenitor/explosion parameter space despite known degeneracies (D. Kasen & S. E. Woosley 2009; L. Dessart & D. J. Hillier 2019; J. A. Goldberg et al. 2019). However, ^{56}Ni mixing (E. Nakar et al. 2016; A. Kozyreva et al. 2019; A. Singh et al. 2019) and SN ejecta interaction with intervening circumstellar material (CSM; D. J. Hillier & L. Dessart 2019; T. Matsumoto et al. 2025) can also impact the plateau phase.

As the ejecta turn optically thin (i.e., the nebular phase), SNe II settle on their light-curve "tail" wherein the standard power source is the radioactive decay of $^{56}\mathrm{Ni} \rightarrow {}^{56}\mathrm{Co} \rightarrow {}^{56}\mathrm{Fe}$ (W. D. Arnett 1982). Modeling of this postplateau decline rate and luminosity allows for observational constraints on the total amount of ^{56}Ni synthesized in explosive nucleosynthesis (J. P. Anderson 2019; L. Martinez et al. 2022b). Based on SN II simulations, the total amount of ^{56}Ni created after core collapse is highly dependent on the explosion energy as well as the progenitor's core structure, mass, and composition (T. Sukhbold et al. 2016; A. Burrows & D. Vartanyan 2021; S. Curtis et al. 2021; E. Laplace et al. 2021; A. Burrows et al. 2024; H. T. Janka 2025). However, construction of more three-dimensional (3D), end-to-end core-collapse SN simulations is necessary to understand consistencies with the observed distributions of SN II observables, in particular ^{56}Ni mass (D. Vartanyan et al. 2025). In addition to the late-time light curve, nebular spectra are another powerful probe of the progenitor's identity and its core mass prior to explosion (A. Jerkstrand et al. 2014; L. Dessart et al. 2021). SN II progenitor zero-age main-sequence (ZAMS) mass is also estimated from direct detection of RSGs in pre-explosion imaging (e.g., S. J. Smartt 2009; B. Davies & E. R. Beasor 2018; E. R. Beasor et al. 2025). Moreover, while radioactive decay is expected to be the main modulator of SN II late-time luminosity, additional energy injection from the persistent collision of SN ejecta with distant CSM can lead to a flattening of the light curve and enhanced UV emission (C. Fransson et al. 2005; J. E. Andrews et al. 2010; K. E. Weil et al. 2020; L. Dessart et al. 2023). Consequently, monitoring of CSM-interacting SNe II at years to decades postexplosion is a direct tracer of the RSG mass-loss history in the final centuries to millennia before core collapse.

To date, many large sample studies have attempted to constrain the SN II progenitor parameter space using the observables described above (e.g., S. Valenti et al. 2016; C. P. Gutiérrez et al. 2017a, 2017b; J. A. Goldberg et al. 2019; J. A. Goldberg & L. Bildsten 2020; L. Martinez et al. 2022a). However, such works do not use information gained about the CSM from very early-time (<2 days after first light) spectra as an additional prior that can be used to differentiate between objects included in SN II samples. However, we now know that a significant fraction (possibly >40%; R. J. Bruch et al. 2023) of SNe II show narrow, high-ionization emission lines in their early-time spectra (i.e., "IIn-like" or "flash" features) from the collision of SN ejecta with confined, dense CSM created in the final years before core collapse (D. C. Leonard et al. 2000; A. Fassia et al. 2001; A. Gal-Yam et al. 2014; D. Khazov et al. 2016; L. Dessart et al. 2017; O. Yaron et al. 2017; R. J. Bruch et al. 2021; W. V. Jacobson-Galán et al. 2024a). Consequently, SNe II with confined CSM are likely typical in samples of SNe II, which could have a significant impact on the correlations inferred from observables.

Intriguingly, SNe II with IIn-like features are best modeled by progenitor mass-loss rates of 10^{-3}–$10^{-1}\,M_{\odot}$ yr^{-1} (e.g., J. H. Groh 2014; I. Shivvers et al. 2015; L. Tartaglia et al. 2021; G. Terreran et al. 2022; K. A. Bostroem et al. 2023; L. Dessart & W. V. Jacobson-Galán 2023; W. V. Jacobson-Galán et al. 2023, 2024b; J. Zhang et al. 2023, 2024; M. Shrestha et al. 2024a; E. A. Zimmerman et al. 2024), which implies CSM densities that are orders of magnitude larger than those inferred for typical SNe II (e.g., T. Szalai et al. 2019; G. Hosseinzadeh et al. 2022; J. Pearson et al. 2023; M. Shrestha et al. 2024b) as well as populations of local RSGs (E. R. Beasor et al. 2020; E. R. Beasor & N. Smith 2022). These enhanced CSM densities close to the progenitor star are also confirmed by early-time radio and X-ray observations of SNe II with IIn-like features (e.g., E. Berger et al. 2023; B. W. Grefenstette et al. 2023;

S. Panjkov et al. 2024; P. Chandra et al. 2024; A. J. Nayana et al. 2025). Given that these SNe evolve to resemble SNe II both photometrically (e.g., light-curve plateau and radioactive-decay tail) and spectroscopically (e.g., Doppler-broadened P-Cygni absorption/emission), it is necessary to understand how the plateau/late-time properties of SNe II with IIn-like features differ from SNe II without early-time CSM interaction. Furthermore, comparison of late-time photometry and spectroscopy to model predictions enables constraints on the types of RSG progenitors associated with CSM-interacting SNe II.

In this paper, we extend the analysis of the SN II sample presented by W. V. Jacobson-Galán et al. (2024a, hereafter WJG24a) to include properties of CSM-interacting SNe II during and after the light-curve plateau phase. In Section 2, we present specifics of the sample and additional late-time spectroscopy to be included in this study. Section 3 presents an analysis of the plateau phase, radioactive-decay decline, and nebular spectra of SNe II with and without IIn-like features. Our results are discussed in Section 4 and our conclusions are drawn in Section 5. All phases reported in this paper are with respect to the adopted time of first light (WJG24a) and are in rest-frame days. When possible, we use redshift-independent host-galaxy distances and adopt standard ΛCDM cosmology ($H_0 = 70$ km s^{-1} Mpc^{-1}, $\Omega_M = 0.27$, $\Omega_\Lambda = 0.73$; Planck Collaboration et al. 2020) if only redshift information is available for a given object.

2. Observations

This work utilizes the same sample of 74 SNe II originally published by WJG24a. The sample includes 39 objects with IIn-like features in their early-time ($t < 10$ days) spectra and 35 SNe II with spectra obtained at $t < 2$ days but showing no detectable IIn-like features (i.e., the "comparison sample"). For objects with IIn-like features, we divide the total sample into two subsamples: "gold-sample" events having spectra at $t < 2$ days and "silver-sample" events only having spectra at $t > 2$ days. As in WJG24a, gold/silver objects are placed in three classes based on the properties of their IIn-like features: "Class 1" objects (plotted in blue) show narrow, high-ionization emission lines of N III, He II, and C IV; "Class 2" objects (plotted in yellow) have no N III emission but do exhibit He II and C IV; and "Class 3" objects (plotted in red) only show weaker, narrow He II emission superimposed on a blueshifted, Doppler-broadened He II line. Finally, when performing statistical tests, we only include SNe with distances $D > 40$ Mpc in order to obtain consistent distance/redshift distributions among all subsamples.

We adopt the sample multiband and pseudobolometric light curves presented by WJG24a in our analysis of the later-phase photometric evolution of all sample objects. Additional variations of the pseudobolometric light curves are generated for the ^{56}Ni mass estimates (e.g., Section 3.2). In addition to the photospheric-phase spectra presented by WJG24a, we now include nebular spectra of gold-, silver-, and comparison-sample objects (e.g., Section 3.4). Nebular spectra were obtained with the Kast spectrograph on the 3 m Shane telescope at Lick Observatory (J. S. Miller & R. P. S. Stone 1994) and Keck/LRIS (J. B. Oke et al. 1995). For all of these spectroscopic observations, standard CCD processing and spectrum extraction were accomplished with IRAF.[42] The data were extracted using the optimal algorithm of K. Horne (1986). Low-order polynomial fits to calibration-lamp spectra were used to establish the wavelength scale and small adjustments derived from night-sky lines in the object frames were applied. Additional spectra were obtained with Keck/DEIMOS, Binospec on the MMT (D. Fabricant et al. 2019), and Gemini Multi-Object Spectrographs (GMOS). These spectroscopic observations were reduced with a variety of pipelines, such as `Pypeit` (J. Prochaska et al. 2020), `Lpipe` (D. A. Perley 2019), and `DRAGONS` (K. Labrie et al. 2019). A log of previously unpublished observations is presented in Table A1.

[42] https://github.com/msiebert1/UCSC_spectral_pipeline

3. Analysis

3.1. Photospheric Phase Light-curve Properties

We present the complete pseudobolometric and *r*-band light curves for gold-, silver-, and control-sample objects in Figure 1. For a number of events in each subsample, we are able to estimate the plateau (i.e., "photospheric-phase") luminosity, duration, and decline rate during this phase. Similar to other sample studies of SNe II (e.g., J. P. Anderson et al. 2014; S. Valenti et al. 2016; R. S. Teja et al. 2024; Q. Fang et al. 2025), we attempt to measure specific parameters that define the light-curve photospheric phase for all objects where the observations allow it. As shown in the upper-left panel of Figure 2, we measure the pseudobolometric luminosity at $t = 50$ days (L_{50}), the light-curve slope at $t = 50$ days (S_{50}), and the photospheric-phase duration as inferred from the fitting function $y(t)$ (e.g., S. Valenti et al. 2016). The L_{50} and S_{50} parameters are calculated through a linear function fit to the light-curve plateau, while t_{PT} is measured after fitting the light curve with the $y(t)$ function. We present these quantities for each class in the gold/silver samples (37 out of 39 objects) as well as the comparison sample (31 out of 35 objects) in Figure 2. Notably, SNe II with IIn-like features display steeper light curves (i.e., "IIL-like"; S. I. Blinnikov & O. S. Bartunov 1993; F. Patat et al. 1994) than comparison-sample objects during the photospheric phase in addition to being more luminous than SNe II without any IIn-like features. However, there is no obvious correlation present when comparing L_{50} to the plateau duration; gold/silver-sample objects show a significant diversity in plateau durations, similar to comparison-sample objects. It is worth noting that for the objects with constrained (i.e., not lower limits) plateau durations, seven SNe II with IIn-like features have $t_{PT} < 80$ days (SNe PTF10abyy, 2017ahn, 2021afkk, 2021can, 2021ont, 2020lfn, and 2021aaqn), with only one comparison-sample object (SN 2020jfo) having such a short plateau duration. Furthermore, six (three detections, three lower limits) gold-sample objects have plateau durations >130 days (SNe 2021aek, 2021dbg, 2021tyw, 2021zj, 2022pgf, and 2016blz), with no comparison-sample objects showing such long plateau durations. Given that this sample is not volume-limited, we are unable to confirm the theoretical rate of short plateau SNe II (e.g., J. J. Eldridge et al. 2018; D. Hiramatsu et al. 2021b). We discuss the physical interpretation of these photospheric-phase properties in Section 4.

Similar to the pseudobolometric light curves, we measure the plateau brightness and decline rate in the *g* (32 gold/silver and 30 comparison) and *r* bands (37 gold/silver and 32 comparison). As shown in Figure 3, there also exists a trend

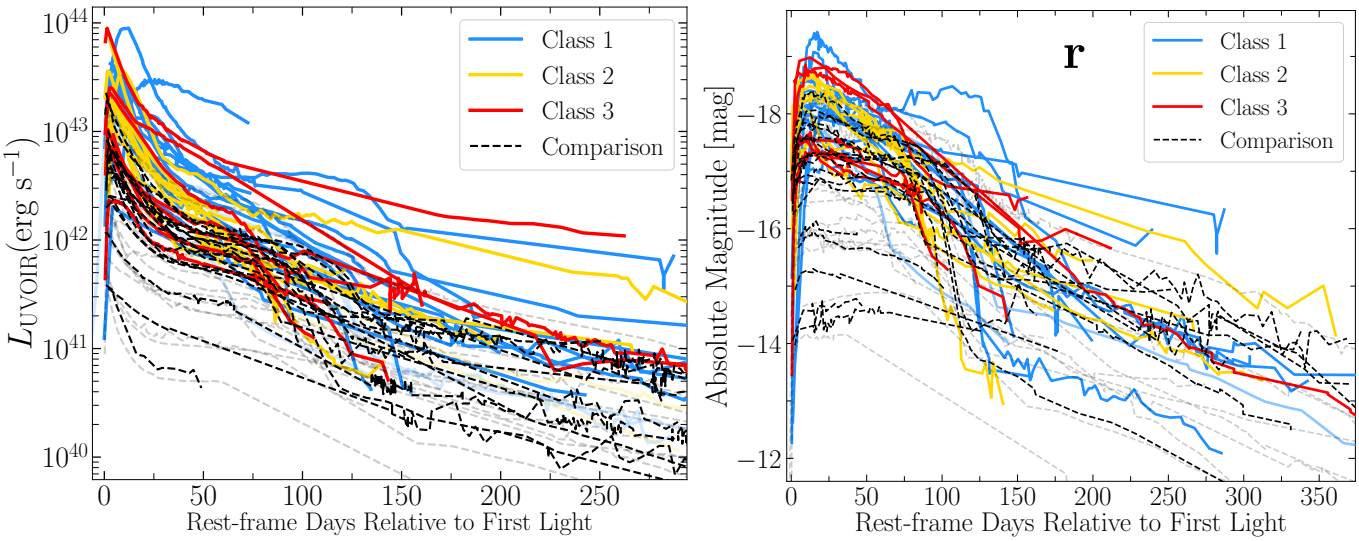

Figure 1. Left: Pseudobolometric (i.e., UVOIR) light curves of gold/silver samples (blue/yellow/red solid lines) and the comparison sample (dashed black lines). Solid black and colored points/curves represent the subsample of objects at $D > 40$ Mpc. Objects at $D < 40$ Mpc are plotted as lower opacity curves/points. Right: Extinction-corrected r-band light curves of gold/silver- and comparison-sample objects. Compared to SNe II without IIn-like features (i.e., comparison sample), objects with confirmed IIn-like signatures are more luminous during the plateau phase.

between the absolute magnitude and decline rate at $t = 50$ days: gold/silver-sample objects are the most luminous and fast-declining during their plateau evolution compared to comparison-sample objects. We present cumulative distributions of the plateau brightness and decline rate at $t = 50$ days in g and r in Figure 3. As shown in Figure 4, all comparison-sample events have a similar $g - r$ color at $t = 50$ days. While some gold/silver-sample objects also show consistent colors at this phase, a number of SNe II with IIn-like features are bluer than normal SNe II at the same phase, which could be the result of subdominant but still significant CSM-interaction power contributing to the SN spectral energy distribution (SED) at later-time phases (L. Dessart & D. J. Hillier 2022). Furthermore, we present all light-curve parameters discussed above with respect to the IIn-like feature timescale in Figure 5.

To test our null hypothesis of whether these sample observables come from the same parent distribution, we apply a logrank test for (i) gold/silver versus comparison samples, (ii) gold/silver-sample Classes 1 and 2 versus 3, and (iii) gold/silver-sample Classes 1 versus 3. These tests are only performed on the subsample of objects where $D > 40$ Mpc. For (i), the chance probability that values of the gold/silver and comparison samples come from the same distribution is $<10^{-3}$% for L_{50}, 0.24% for $M_{g,50}$, and 0.11% for $M_{r,50}$. We find that S_{50} for pseudobolometric, g, and r between samples belong to the same distribution at the 0.01%, 6×10^{-4}%, and 0.02% levels, respectively. For (ii), the null-hypothesis probability for pseudobolometric, g, and r brightness (decline rate) at $t = 50$ days is 76.8(33.9)%, 13.7(2.9)%, and 17.9 (27.2)%, respectively. For (iii), the null-hypothesis probability for pseudobolometric, g, and r brightness (decline rate) at $t = 50$ days is 47.1(60.2)%, 13.0(11.9)%, and 33.8(74.1)%, respectively. Therefore, we confirm that all classes in the gold/silver samples are more luminous and decline faster on the plateau than comparison-sample objects. However, we find no statistically significant differences for these parameters between classes in the gold/silver samples.

3.2. ^{56}Ni Masses

In noninteracting SNe II, the main power source for the ejecta is radioactive decay, of which the ^{56}Co $\rightarrow$ ^{56}Fe (W. D. Arnett 1982) chain dominates at the epochs of 100–350 days studied here. In this section, we first assume that the only power source for the whole sample of objects is ^{56}Ni decay power before demonstrating that this assumption breaks down for a number of objects with clear signs of late-time CSM interaction. In this framework of an exclusive decay power source, both the total mass of ^{56}Ni present in the SN as well as the timescale of γ-ray escape (t_γ) can be measured by modeling the bolometric luminosity evolution postplateau (e.g., E. Cappellaro et al. 1997; A. Clocchiatti & J. C. Wheeler 1997; S. Valenti et al. 2008; J. C. Wheeler et al. 2015; W. V. Jacobson-Galán et al. 2021). However, to properly utilize the analytic formalisms for radioactive-decay power, the bolometric light curve should be constructed with multi-band photometry that covers ultraviolet (UV) through infrared (IR) wavelengths. Given that the pseudobolometric light curves presented in this Figure 1 only include UV through optical/near-IR wavelengths, all resulting measurements of $M(^{56}\mathrm{Ni})$ will be underestimates of the true amount of synthesized radioactive material powering the SN light curve. We do not construct the late-time bolometric light curve through fitting of the SED with a blackbody model because during postplateau phases the SN spectrum will transition to the nebular phase (i.e., emission-line dominated) and therefore a blackbody approximation is no longer appropriate. We note that ^{56}Ni mass in SNe II may also be inferred from the light-curve steepness during the transition from plateau to radioactive decline powered tail (e.g., see A. Elmhamdi et al. 2003; A. Singh et al. 2018), but this method can be influenced by ejecta properties such as densities, chemical mixing, and asymmetries.

To measure $M(^{56}\mathrm{Ni})$ and t_γ in gold/silver- and comparison-sample objects, we compare to the pseudobolometric light curve of SN 1987A, as has been done in previous SN II sample studies (e.g., S. Spiro et al. 2014; S. Valenti et al. 2016). To do this, we construct new pseudobolometric light curves using

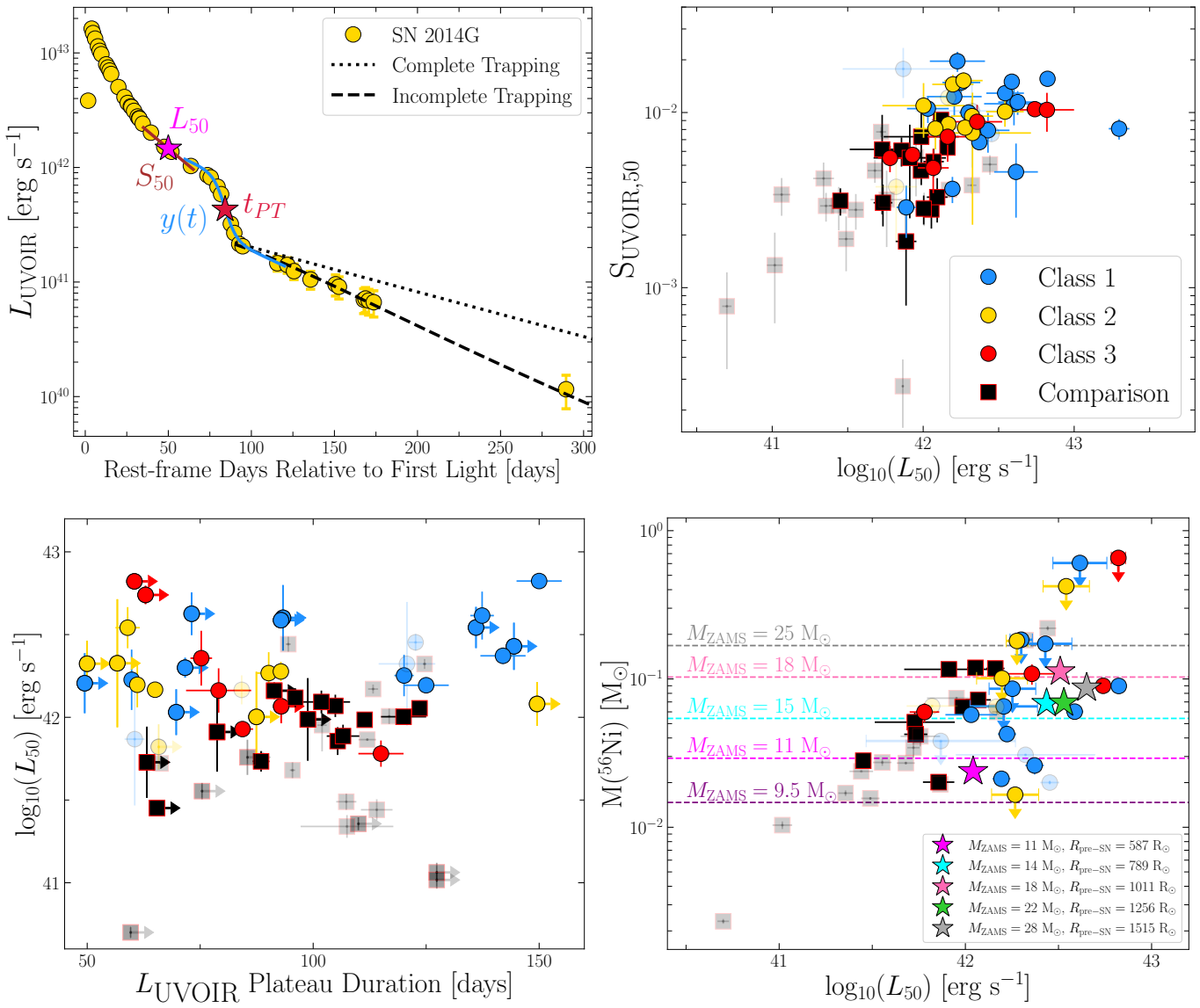

Figure 2. Top left: Pseudobolometric light curve of Class 2 object SN 2014G (yellow circles) with light-curve parameters derived for all sample objects (Section 3.1) labeled for visualization: the luminosity at 50 days (L_{50}, magenta star), light-curve decline rate at 50 days (S_{50}, brown solid line), photospheric-phase duration ($t_{\rm PT}$, red star), and Fermi–Dirac function ($y(t)$, solid blue line). Additionally, radioactive-decay powered models for complete and incomplete γ-ray trapping are plotted as dotted and dashed black lines. Top right: Pseudobolometric light-curve luminosity and decline rate at $t = 50$ days for gold/silver- (blue, yellow, red circles) and comparison-sample (black squares) objects. SNe II with IIn-like features are more luminous and decline faster during their photospheric phase. Solid colored points/curves represent the subsample of objects at $D > 40$ Mpc. Bottom left: Luminosity at 50 days (L_{50}) vs. photospheric-phase duration. Bottom right: ^{56}Ni mass vs. pseudobolometric luminosity at +50 days. Theoretical predictions for ^{56}Ni yields from 9.5 to 25 $M_\odot$ (A. Burrows et al. 2024) progenitor models shown as dashed lines and 11–28 $M_\odot$ (S. Curtis et al. 2021) progenitor models shown as stars.

combinations of optical filters (e.g., *gri*, *UBVRI*, *BVgri*, etc.) and fit these light curves with the pseudobolometric light curve of SN 1987A derived with the same filter combination (see N. Meza-Retamal et al. 2024 for more information). This SN 1987A light-curve model is represented in the form

$$\frac{L_{\rm pbol}(t)}{L^{\rm 87A}_{\rm pbol}(t)} = \left(\frac{M_{^{56}\rm Ni}}{0.075}\right)\left(\frac{1-\exp(-(t_\gamma/t)^2)}{1-\exp(-(540/t)^2)}\right), \quad (1)$$

where t is time in days postexplosion, $L_{\rm pbol}$ is the pseudobolometric luminosity, and the SN 1987A γ-ray trapping timescale is 540 days (N. B. Suntzeff & P. Bouchet 1990).

We present measured $M(^{56}$Ni) values for gold/silver (24 out of 39 objects) and comparison samples (24 out of 39 objects) in Figure 2 and Tables A2 and A3. Similar to past studies (e.g., M. Hamuy 2003; S. Spiro et al. 2014; O. Pejcha & J. L. Prieto 2015; S. Valenti et al. 2015), there is a visible trend between $M(^{56}$Ni) and L_{50} where more luminous SNe II also produce more ^{56}Ni. However, a number of SNe II with IIn-like features in the gold/silver samples break this correlation with their high L_{50} but low/moderate $M(^{56}$Ni) values. This might imply that there is another parameter related to the progenitor star and/or the explosion itself that can account for this deviation (e.g., see Section 3.6 for more discussion). As shown in Figure 2, there are a number of SNe II in both gold/silver and comparison samples that have $M(^{56}$Ni) $> 0.1\,M_\odot$—this being consistent with theoretical predictions for SNe II from extremely large ($>18\,M_\odot$) RSGs by S. Curtis et al. (2021) and A. Burrows et al. (2024). To confirm that these values are accurate, we explore the

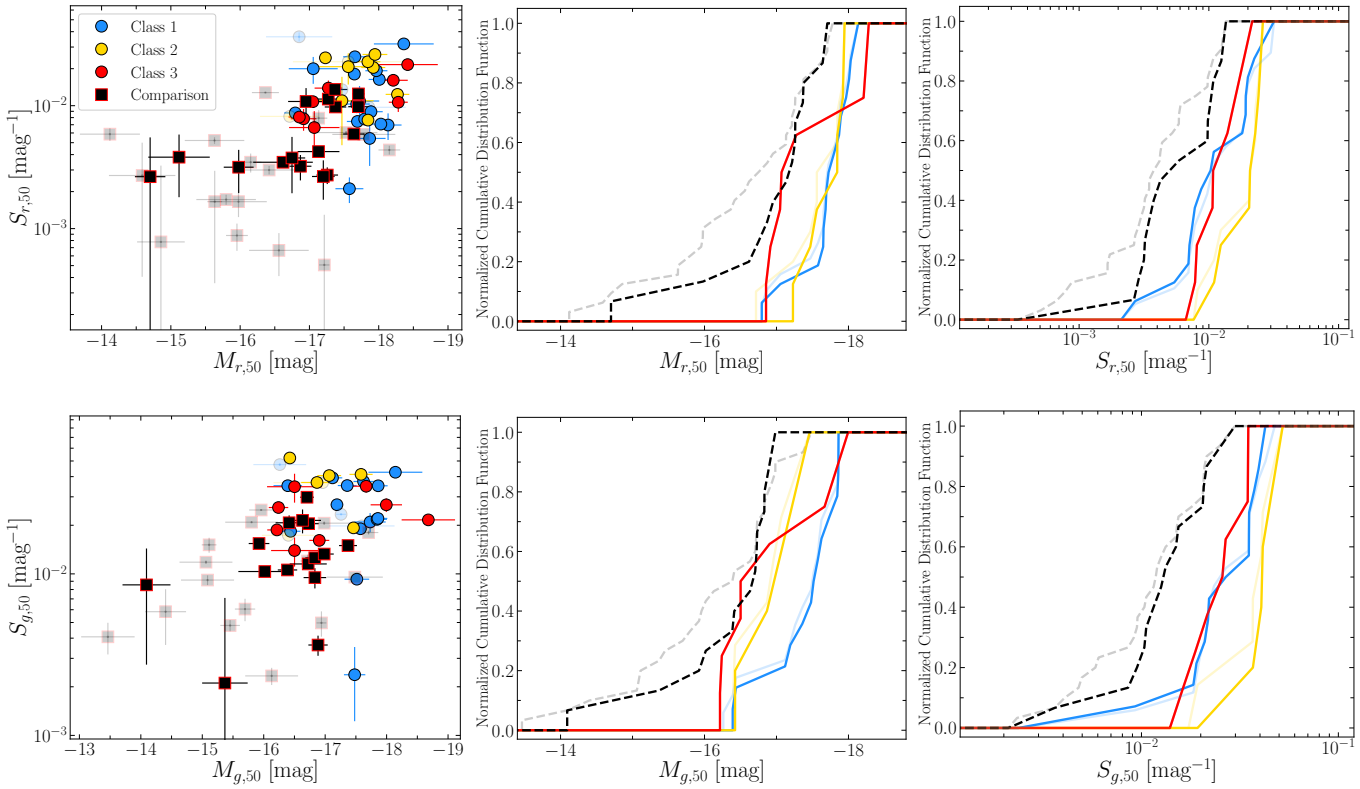

Figure 3. Light-curve decline rate vs. absolute magnitude at 50 days for *r*- (top panel) and *g*-band (bottom panel) light curves. Solid colored points/curves represent the subsample of objects at $D > 40$ Mpc. Cumulative distributions of *r*- (top panel) and *g*-band (bottom panel) light-curve parameters shown for comparison- (black dashed lines) and gold/silver-sample (solid blue, yellow and red lines) objects. SNe II with IIn-like features have a distinct distribution of S_{50} and M_{50} compared to comparison-sample objects.

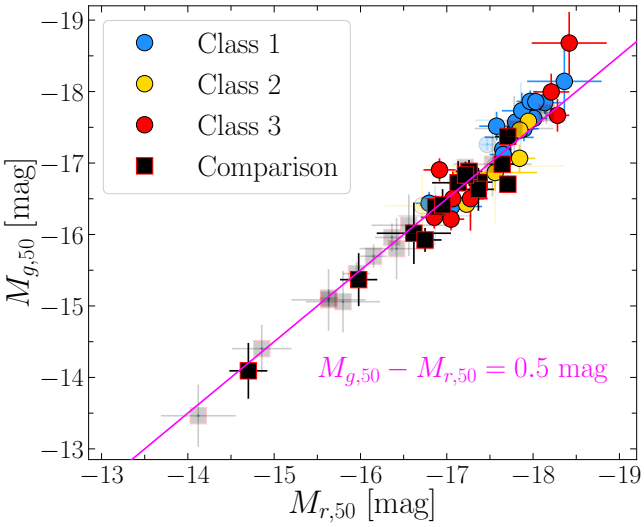

Figure 4. Absolute *g*- and *r*-band magnitudes at +50 days for gold/silver- (blue, yellow, and red circles) and comparison-sample (black squares) objects. M_g–$M_r = 0.5$ mag color difference shown as magenta line. Some brighter SNe II with IIn-like features show bluer colors during the plateau phase, possibly revealing extra heating from ongoing CSM interaction.

possibility that the pseudobolometric light curves were over-corrected for host-galaxy extinction (e.g., see Appendix discussion of WJG24a) by plotting $E(B-V)_{\rm host}$ values versus $M(^{56}{\rm Ni})$ for all objects in Appendix Figure A1. Similar to comparison of $E(B-V)_{\rm host}$ with L_{50} and $M_{r,50}$ measurements, there is no obvious correlation between $M(^{56}{\rm Ni})$ and the adopted host-galaxy extinction; SNe II with high $M(^{56}{\rm Ni})$ span a range of $E(B-V)_{\rm host}$ values. Nevertheless, because of the general uncertainty in accurately measuring host extinction, objects with both high $M(^{56}{\rm Ni})$ and $E(B-V)_{\rm host}$ values should be interpreted with caution, and it is advisable to treat their ^{56}Ni masses as upper limits.

Another source of uncertainty in measuring $M(^{56}{\rm Ni})$ is the potential for non-negligible luminosity arising from ongoing CSM interaction. For a shock wave with velocity $v_{\rm sh}$ propagating through a steady-state wind (i.e., $\rho \quad r^{-2}$) with mass-loss rate $\dot{M}$ and velocity v_w, the power supply of the shocks goes as $L_{\rm sh} = \dot{M} v_{\rm sh}^3 / 2 v_w$. Consequently, for even a weak RSG mass-loss rate of $\dot{M} \approx 10^{-6}\,M_\odot$ yr^{-1} ($v_{\rm sh} = 10^4$ km s^{-1}, $v_w = 30$ km s^{-1}), the resulting shock power is quite large ($L_{\rm sh} \quad 10^{40}$ erg s^{-1}). This shock power is likely radiated by the reverse shock as it deposits energy into the cold dense shell (CDS) in the form of X-rays from free–free emission following conversion of kinetic to thermal energy in the postshock gas (T. K. Nymark et al. 2006; R. A. Chevalier & C. Fransson 2017; L. Dessart & D. J. Hillier 2022). The CDS can be formed soon after shock breakout if there is confined, high-density CSM (e.g., $0.1\,M_\odot$ is expected for SNe II with IIn-like features) or later in the SN evolution as more CSM is swept up (e.g., $M_{\rm CDS} = 10^{-3}\,M_\odot$ at 1 yr for $\dot{M} = 10^{-6}\,M_\odot$ yr^{-1}, $v_w = 10$ km s^{-1} and $v_{\rm sh} = 10^4$ km s^{-1}; L. Dessart & D. J. Hillier 2022). If the distant CSM has sufficiently high density, the shock power could contribute significantly to the pseudobolometric luminosities used to measure $M(^{56}{\rm Ni})$ and the derived masses would only be considered upper limits on the true amount of radioactive material present in the SN. This is demonstrated in Figure 6, where we show that modeling pseudobolometric light curves derived from only optical photometry with Equation (1) can lead

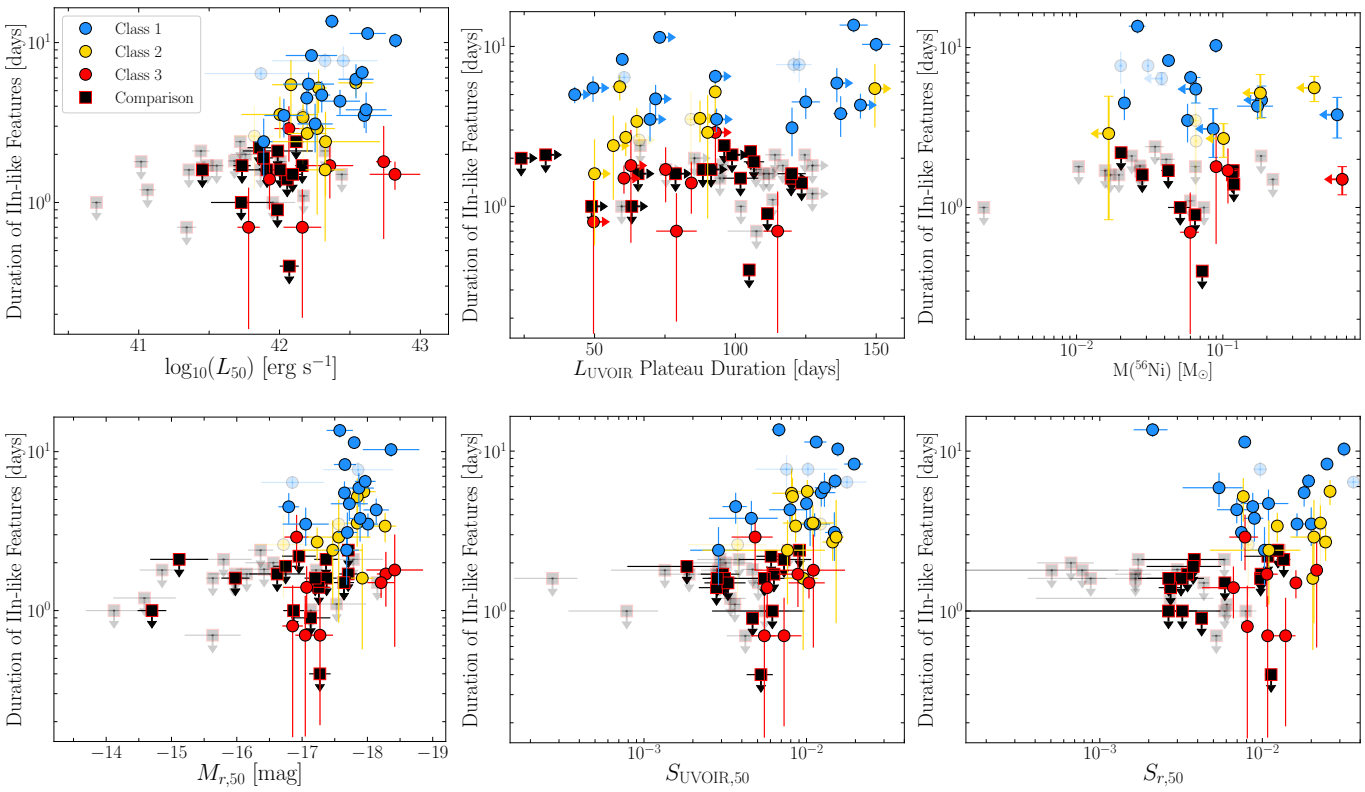

Figure 5. Duration of IIn-like features for gold/silver- (blue, yellow, red circles) and comparison-sample (black squares) objects vs. L_{50}, t_{pl}, and $M(^{56}\mathrm{Ni})$ (top panel), and $M_{r,50}$, $S_{\mathrm{UV\ OIR},50}$, and $S_{r,50}$ (bottom panel). SNe II with IIn-like features have statistically distinct distributions for plateau brightness and decline rate but not for ^{56}Ni mass or plateau duration.

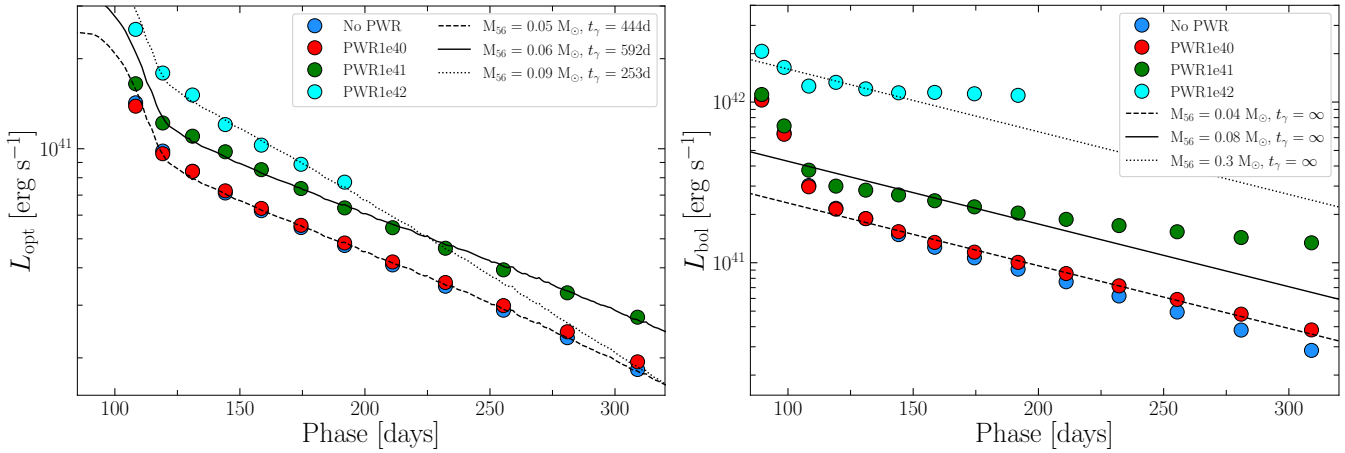

Figure 6. Left: Postplateau pseudobolometric light curves from L. Dessart & D. J. Hillier (2022) derived from 3000 to 10000 Å(circles), all of which have the same M(^{56}Ni) but with varying amounts of shock power. Fitting the analytic formalism for SN 1987A (e.g., Equation (1)) returns the model $M(^{56}\mathrm{Ni})$ correctly for no shock power and $L_{\mathrm{sh}} = 10^{40}$ erg s^{-1}, but the $M(^{56}\mathrm{Ni})$ is overestimated if the shock power is $\geqslant 10^{41}$ erg s^{-1}. Right: Complete bolometric light curves for shock-power models compared to radioactive-decay power models. The influence of shock power across the SN SED, in particular in the UV, will cause a significant overprediction of $M(^{56}\mathrm{Ni})$ when modeling the late-time light curve.

to a significant overestimation of the ^{56}Ni mass if a shock power of $>10^{40}$ erg s^{-1} is present (L. Dessart & D. J. Hillier 2022).

To explore this effect in more detail, we examine the late-time photometric and spectroscopic behavior of all sample objects with large ^{56}Ni masses (e.g., $M(^{56}\mathrm{Ni}) > 0.08\,M_{\odot}$). Among the gold/silver events with high $M(^{56}\mathrm{Ni})$, SNe 2020abjq, 2021zj, 2021can, 2022dml, 2021ont, and PTF11iqb show spectroscopic signatures of significant shock power in both their photospheric and late-time spectra (Figures 7 and 8), which will be responsible for overestimating $M(^{56}\mathrm{Ni})$. Consequently, we present $M(^{56}\mathrm{Ni})$ for these objects as upper limits (e.g., Figure 2). Additionally, it is worth noting that other events (e.g., SNe 2017ahn, 2020pni, and 2014G) with more typical $M(^{56}\mathrm{Ni})$ estimates also exhibit broad/boxy H emission during their radioactive-decay decline phase. This indicates that $M(^{56}\mathrm{Ni})$ could be overestimated in many events due to a non-negligible contribution from shock power, which

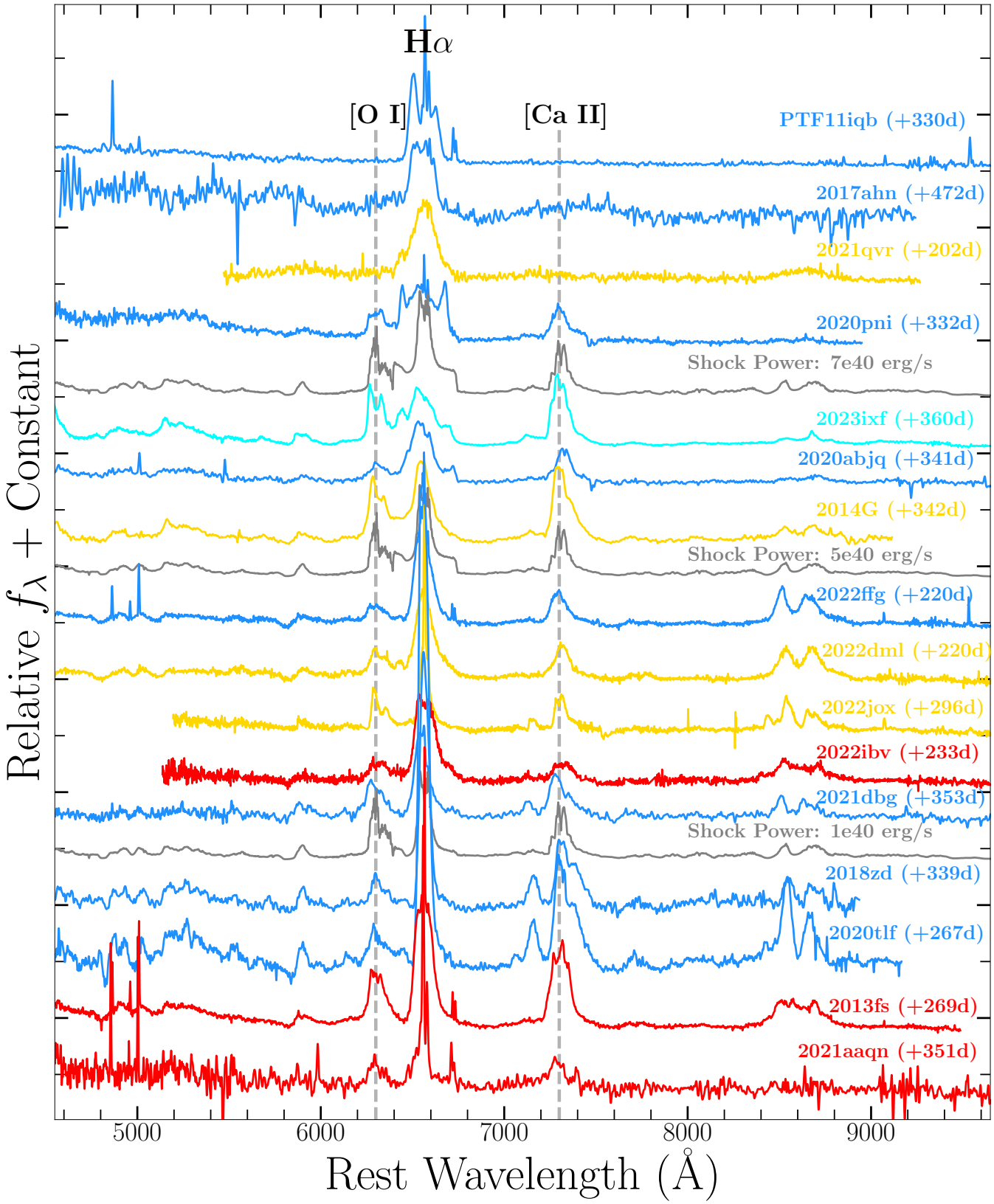

Figure 7. Nebular spectra of gold/silver-sample objects (blue, yellow, red), SN 2023ixf (cyan), and CMFGEN shock-power models from L. Dessart & D. J. Hillier (2022). Spectra are presented in order of decreasing spectroscopic evidence for ongoing CSM interaction (e.g., boxy H emission) from top to bottom.

can only be confirmed by continuous spectroscopic monitoring out to late-time phases. More discussion of the detection of ongoing, late-time CSM interaction is presented in Section 4.2.

3.3. γ-Ray Trapping

In addition to $M(^{56}\mathrm{Ni})$, we are able to measure t_γ values that indicate incomplete γ-ray trapping in a number of sample

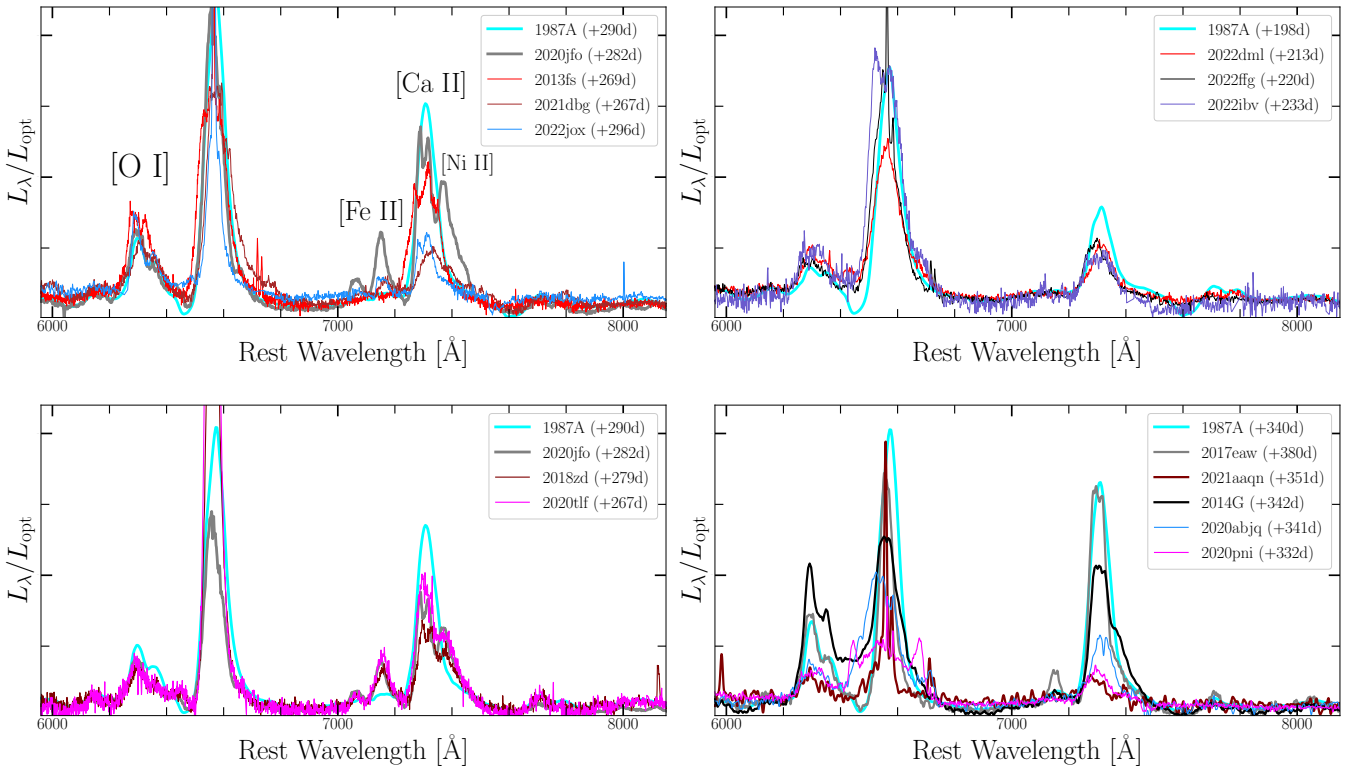

Figure 8. Upper left: Nebular spectra comparison of SNe 1987A (cyan) and 2020jfo (gray) with gold/silver-sample SNe 2021dbg (brown), 2022jox (blue), and 2013fs (red). All spectra have been normalized by the integral of the optical spectrum in the range 5000–9000 Å. Upper right: SN 1987A (cyan) compared with gold/silver-sample SNe 2022dml (red), 2022ffg (black), and 2022ibv (turquoise). Lower left: SNe 1987A (cyan) and 2020jfo (gray) compared with gold/silver-sample SNe 2018zd (purple) and 2020tlf (magenta). Notably, these gold/silver-sample objects have weaker [O I] emission than comparison SNe. Lower right: SNe 1987A (cyan) and 2017eaw (gray) compared with gold/silver-sample SNe 2014G (black), 2020abjq (blue), 2020pni (magenta), and 2021aaqn (brown). These gold/silver-sample objects are examples where the dense-shell emission is forming a "boxy" profile within the H complex, which is a product of ongoing interaction with distant, relatively dense CSM.

objects. As shown in Tables A2 and A3, most gold/silver- and comparison-sample objects with measured $M(^{56}\mathrm{Ni})$ have trapping timescales >450 days and/or are consistent with complete γ-ray trapping. However, there are eight gold/silver and eight comparison-sample objects with constrained t_γ values of <400 days, some even as low as 200 days. Incomplete γ-ray trapping has interesting implications for SN ejecta mass and kinetic energy as shown in the analytic formalism from A. Clocchiatti & J. C. Wheeler (1997), which is typically applied to Type Ib/c or Ia SNe. Here, $t_\gamma = (C(\eta)\kappa_\gamma M_{ej}^2 E_k^{-1})^{0.5}$, where $C(\eta)$ is the density function, κ_γ is the γ-ray opacity (0.048 cm^2 g^{-1} for H-rich ejecta), M_{ej} is the ejecta mass, and E_k is the kinetic energy. Assuming a flat density profile (i.e., $\eta = 0$) and a fiducial kinetic energy of 1 B, t_γ values in the range 200–400 days would imply ejecta masses of 4.7–9.3 $M_\odot$. However, the analytic expression from A. Clocchiatti & J. C. Wheeler (1997) is a very rough approximation that makes assumptions about spherical symmetry and the ejecta density profile that ignore known complexities about the "Nickel bubble effect" and clumping (e.g., M. Basko 1994; L. Dessart & E. Audit 2019; L. Dessart et al. 2021; M. Gabler et al. 2021). Nevertheless, sample objects with $t_\gamma < 250$ days implies smaller ejecta masses than what is expected from SNe II with minimal envelope removal prior to core collapse. Notably, SNe 2014G, 2017ahn, 2021can, and 2020jfo have $t_\gamma < 200$ days and also have short plateau timescales (<85 days), both of which are consistent with lower ejecta mass values.

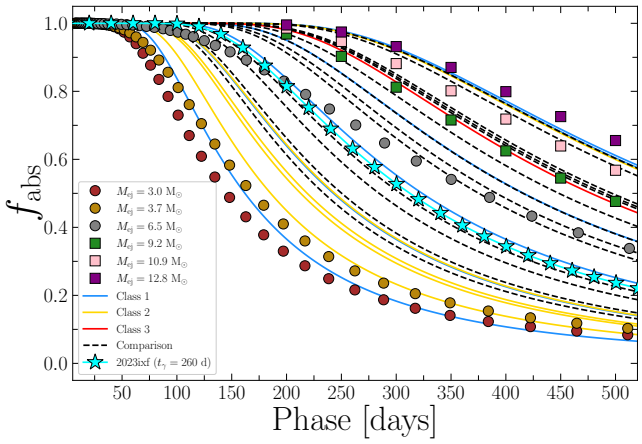

Figure 9. Fraction of radioactive-decay power absorbed in the SN ejecta (f_{abs}) calculated for CMFGEN models of varying ejecta masses (circles and squares) compared to gold/silver- and comparison-sample objects. f_{abs} is estimated for the sample objects using their calculated γ-ray trapping timescales (t_γ). SN 2023ixf is shown for reference as cyan stars.

We explore this in more detail by calculating the fraction of absorbed radioactive-decay power (f_{abs}) for different SN ejecta masses in CMFGEN models for SNe II out to late-time phases. In Figure 9, we plot the f_{abs} for SN II models from L. Dessart et al. (2024) that have ejecta masses of 3–6.5 $M_\odot$ owing to substantial removal of the H envelope from binary interaction —these models have an initial mass of $M_{ZAMS} = 12.6\,M_\odot$. Additionally, we plot more typical SN II models that arise

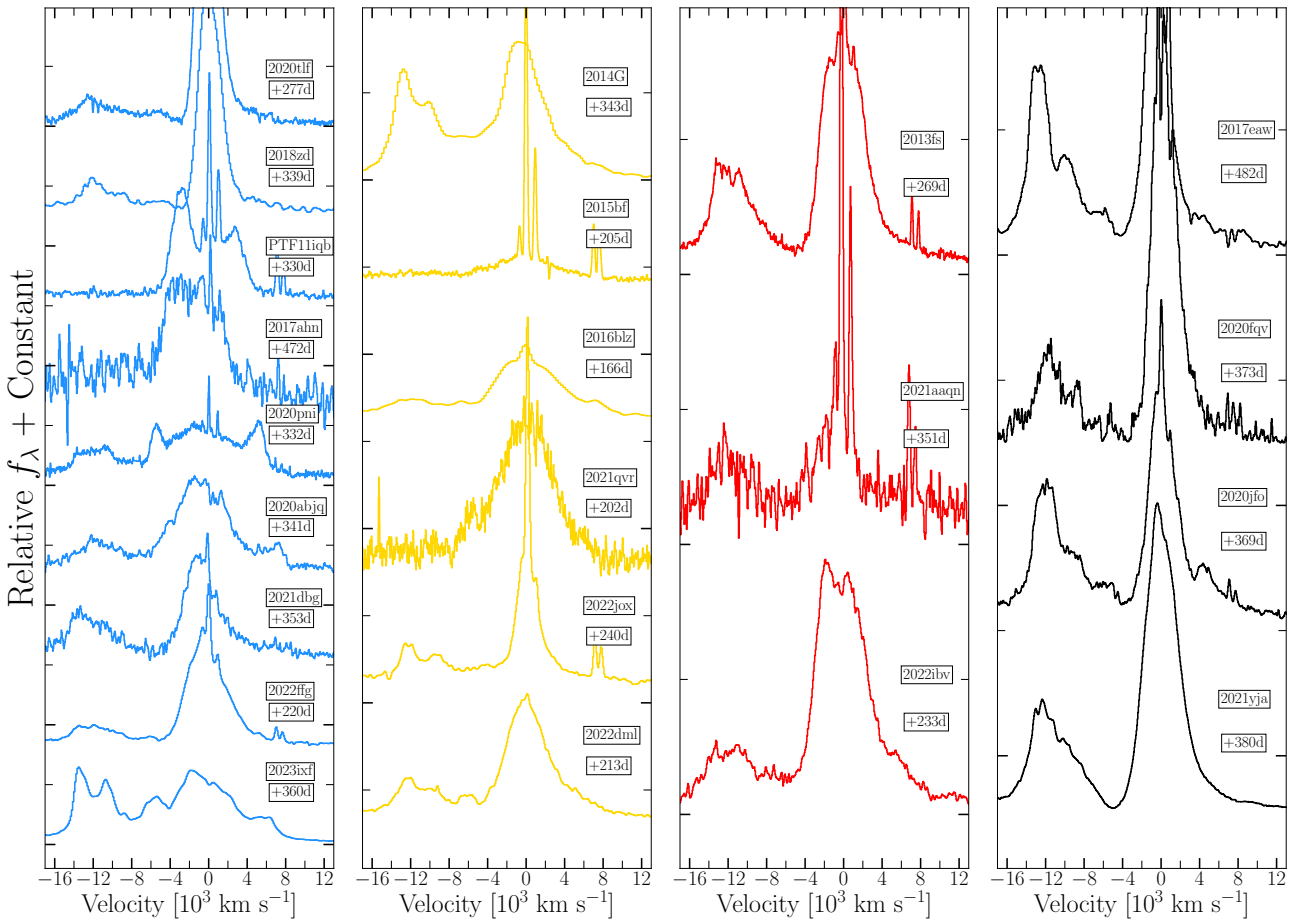

Figure 10. H /[O I] spectral region shown in velocity space relative to H rest wavelength for gold/silver-sample objects shown in blue, yellow, and red as well as four comparison-sample objects shown in black for reference. In addition to the [O I] and H emission from the inner ejecta (narrower components), many SNe II with IIn-like features develop an underlying broad, boxy H profile from emission in a dense shell formed between the forward and reverse shocks. The detection of the dense-shell emission indicates significant contribution from shock power at late times and higher CSM densities (e.g., $>10^{-6}\,M_\odot$ yr^{-1}) at large radii (e.g., $>10^{16}$ cm).

from RSGs with $M_{\rm ZAMS} = 11$–$15\,M_\odot$, which have $M_{\rm ej} = 9.2$–$12.8\,M_\odot$. Both sets of models have kinetic energies of 1–1.3 B. As shown in Figure 9, models with low ejecta masses ($<6.5\,M_\odot$) best match sample objects with $t_\gamma = 200$–300 days, while models with intermediate ejecta masses (6.5–$9.2\,M_\odot$) more resemble SNe II with $t_\gamma = 300$–400 days. Finally, all sample objects consistent with more complete γ-ray trapping (e.g., $t_\gamma > 500$ days) at phases $t < 300$ days are likely best matched by more typical ejecta masses $>11\,M_\odot$. However, as discussed in Section 3.2, there might be significant influence from shock power on the postplateau decline rate, which could induce additional uncertainty on the t_γ estimates in some gold/silver-sample objects. Furthermore, as shown in Figure 1, the late-time light curves of most sample objects only extend to $t < 300$ days—ideally there would be complete, multiband coverage out to 500–600 days post-explosion in order to robustly constrain the γ-ray trapping timescales.

3.4. Nebular Spectroscopy

We present late-time/nebular spectroscopy of gold/silver-sample objects at phases $t = 200$–500 days in Figure 7. We present a log of unpublished nebular spectra in Table A1 and also include previously published late-time spectra for the following objects: SNe PTF11iqb (N. Smith et al. 2015), 2013ab (S. Bose et al. 2015), 2013am (J. Zhang et al. 2014; L. Tomasella et al. 2018), 2013fs (A. Gal-Yam 2017), 2014G (G. Terreran et al. 2016), 2015bf (H. Lin et al. 2021), 2016X (F. Huang et al. 2018), 2016aqf (T. E. Müller-Bravo et al. 2020), 2017ahn (L. Tartaglia et al. 2021), 2017eaw (T. Szalai et al. 2019; K. E. Weil et al. 2020), 2018zd (J. Zhang et al. 2020), 2018cuf (Y. Dong et al. 2021), 2018lab (J. Pearson et al. 2023), 2020fqv (S. Tinyanont et al. 2022), 2020jfo (C. D. Kilpatrick et al. 2023), 2020tlf (W. V. Jacobson-Galán et al. 2022), 2021gmj (N. Meza-Retamal et al. 2024), and 2022jox (J. E. Andrews et al. 2024). In total, this study includes nebular spectroscopy for 19 gold/silver- and 13 comparison-sample objects. We also include late-time spectra of SN 2023ixf (W. V. Jacobson-Galán et al. 2025) for comparison to gold/silver-sample objects. Similar to nebular observations of SNe II without IIn-like features, many early-time CSM-interacting SNe II display strong forbidden emission lines such as [O I] $\lambda\lambda$6300, 6364 and [Ca II] $\lambda\lambda$7291, 7323, as well as prominent H emission. Despite the small number of gold/silver-sample objects with nebular spectra, these SNe display significant spectral diversity at late times, in particular in their [O I]/H complex in the wavelength range 6200–6800 Å.

As shown in Figure 10, the [O I] profile in gold/silver-sample objects is quite diverse: some events show weak/no

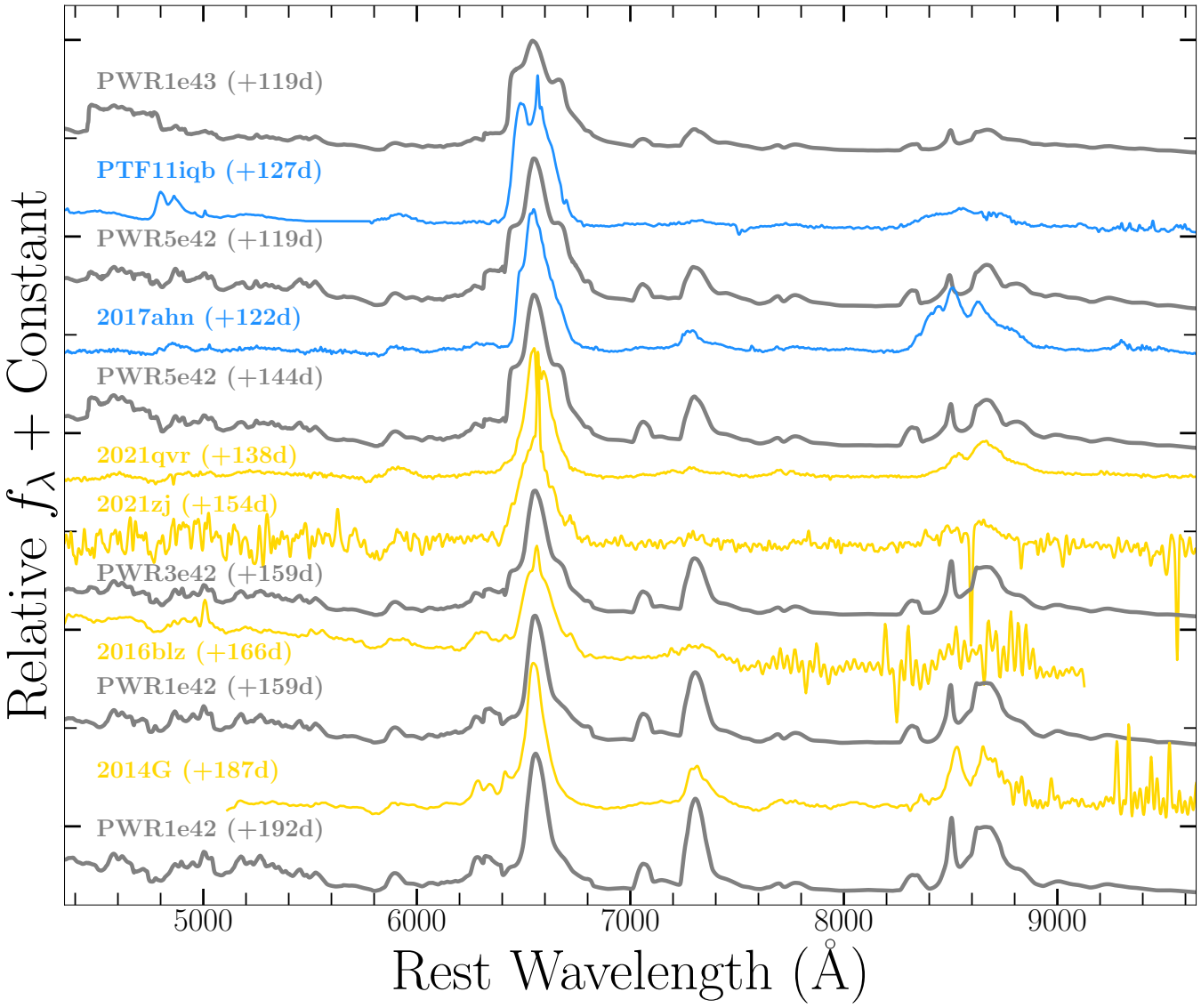

Figure 11. Late-time spectra of gold/silver-sample objects with signatures of significant CSM interaction (blue and yellow spectra) compared to CMFGEN shock-power models from L. Dessart & D. J. Hillier (2022). These SNe II show very weak or no forbidden-line emission and their spectra are dominated by intermediate width H emission from the dense shell formed as the SN shock continues to sweep up significantly high-density CSM at large radii.

emission (e.g., SNe PTF11iqb, 2015bf, 2017ahn, 2018zd, 2020tlf, 2020pni, 2021qvr, and 2022ffg), while others exhibit strong, double-peaked profiles (e.g., SNe 2014G, 2022jox, 2022dml, 2013fs, and 2022ibv). For reference, we also display a zoom-in of the [O I] profile of a subsample of comparison objects (SNe 2017eaw, 2020fqv, 2020jfo, and 2021yja), all of which have prominent forbidden-line emission. Examining the H profile in more detail, we see that there is a potential continuum of late-time CSM-interaction signatures within the Class 1, 2, and 3 objects. For example, SNe like PTF11iqb and SN 2017ahn only show boxy H emission ($v_{\rm max} \approx 4000$ km s^{-1}), which is similar, but likely more extreme, than events like SNe 2016blz and 2021qvr that have both boxy emission ($v_{\rm max} \approx 8000$ km s^{-1}) and a narrower Gaussian profile typical of nebular phases. These objects have weak and/or no detectable forbidden emission lines. Then, there are events such as SNe 2020pni, 2020abjq, 2022ffg, 2014G, 2022jox, 2022dml, and 2022ibv that display standard forbidden lines but show an underlying boxy component within H ($v_{\rm max} \approx 8000$ km s^{-1})—this is similar to the nebular evolution of SN 2023ixf (G. Folatelli et al. 2025; Jacobson-Galán et al 2025, in preparation; A. Kumar et al. 2025; G. Li et al. 2025). We discuss the implications for detecting late-time dense-shell emission in Section 4.2 and illustrate more early-time examples of these interaction signatures in Figure 11, as well as those at later-time phases in Figure 12. Finally, gold/silver-sample SNe 2013fs, 2018zd, 2020tlf, 2021dbg, and 2021aaqn do not show any underlying boxy emission in H , similar to comparison-sample SNe at nebular times.

In Figure 8, we present nebular spectra normalized by their optical luminosities between 5000 and 9000 Å. For gold/silver-sample objects, we compare forbidden-line emission (e.g., [O I] and [Ca II]) to reference objects SNe 1987A, 2017eaw, and 2020jfo at similar phases and find significant spectral diversity. These comparison objects were chosen given the lack of CSM-interaction signatures and their variety of [O I] emission-line strengths. For example, only SNe 2013fs, 2022jox, and 2014G have significantly larger [O I] emission than SNe 1987A or 2020jfo, while the rest of the

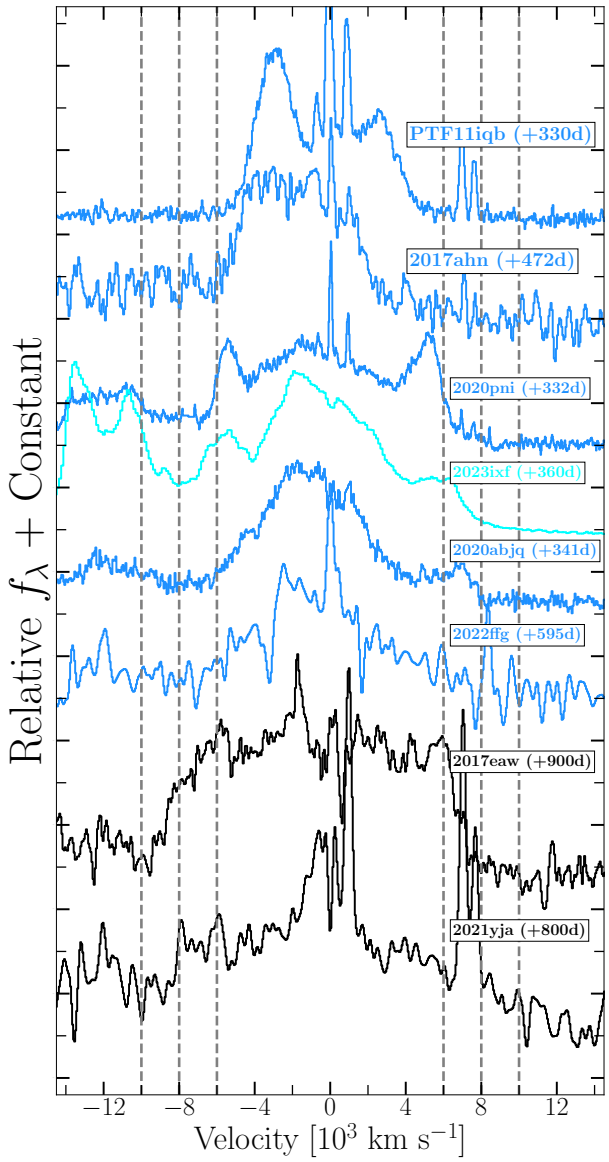

Figure 12. Late-time H velocity for gold/silver- and comparison-sample objects that develop boxy emission from shock power reprocessed by a CDS. The timescales over which this broad, boxy H emission emerges are a tracer of the shock power derived from more distant ($R > 10^{16}$ cm) CSM that is being consistently swept up into the CDS.

subsample have comparable or weaker [O I] luminosities. Applying the common assumption that [O I] is a metric for ZAMS mass (i.e., He core mass), then it is possible that many CSM-interacting SNe II in this come from lower mass stars ($<12\,M_\odot$). Notably, some of these objects (e.g., SNe 2014G, 2020abjq, 2020pni, 2022dml, 2022jox and 2022ibv) also show strong broad, boxy H from emission from the dense shell, which strongly contrasts the typical absorption seen in H of SNe 1987A and 2020jfo. Furthermore, it is intriguing to see similarity between a comparison-sample object such as SN 2020jfo that showed no IIn-like features and gold/silver-sample objects such as SNe 2020tlf and 2018zd—all three objects have nearly perfectly matched [O I]/[Ca II] and even show prominent [Ni II] λ7378 emission, which is proposed to be a signature of lower mass ($<12\,M_\odot$ progenitors) (e.g., A. Jerkstrand et al. 2015). However, the nebular spectra of SNe 2018zd and 2020tlf deviate from SN 2020jfo in their

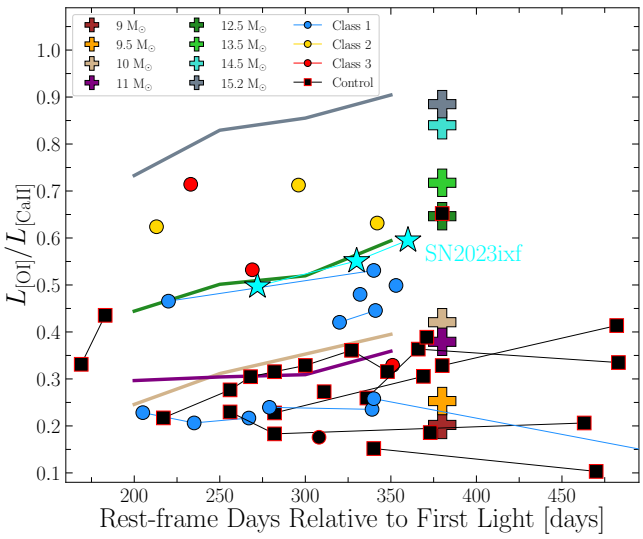

Figure 13. Ratio of [O I] and [Ca II] luminosities for gold/silver- (blue, yellow, red circles) and comparison-sample (black squares) objects. SN 2023ixf is shown as cyan stars. Line ratios for 9–15.2 $M_\odot$ ZAMS models are shown as lines and plus signs (L. Dessart et al. 2021). Compared to model predictions, the majority of SNe II in this sample are consistent with ZAMS masses of $\leqslant$13 $M_\odot$.

incredibly strong H emission, which may also be a signature of a low-mass progenitor star (e.g., L. Dessart et al. 2021). SN 2018zd's consistency with the nebular properties of other SNe II, both with and without IIn-like signatures, as well as the inconsistency with very low-mass model predictions (e.g., $\leqslant$9.5 $M_\odot$) makes it more ambiguous whether SN 2018zd is a true electron-capture SN (e.g., D. Hiramatsu et al. 2021b) or just the core-collapse of a low-mass (e.g., 10–12 $M_\odot$) RSG.

3.5. Progenitor Mass Estimation

Nebular spectroscopy of SNe II provides an additional constraint on the mass of the RSG progenitor star (e.g., A. Jerkstrand et al. 2014; S. Valenti et al. 2016; L. Dessart et al. 2021). In Figure 13, we present the [O I]/[Ca II] line-luminosity ratio as a function of phase for all sample objects with nebular-phase spectroscopy compared to the same measurement for a grid of models for progenitor ZAMS masses of 9–15.2 $M_\odot$ from L. Dessart et al. (2021). For both models and data, we calculate line luminosities by first modeling and subtracting off the continuum emission before measuring the integrated line emission. For objects with boxy H emission that extends into the wavelength range of [O I], we model the forbidden-line emission using two Gaussian profiles centered at 6300 and 6364 Å. We also include line-ratio measurements for SN 2023ixf at late-time phases for comparison to sample objects. While the [O I]/[Ca II] is sensitive to progenitor core mass, we note that it is also dependent on ejecta density, temperature, and clumping, all of which could influence the inferred ZAMS masses (A. Jerkstrand et al. 2014; L. Dessart et al. 2021).

Interestingly, most comparison-sample SNe are consistent with ZAMS masses of 9–11 $M_\odot$, as are Class 1 SNe 2018zd and 2020tlf and Class 3 SN 2021aaqn. Similarly, gold/silver-sample SNe 2013fs, 2014G, 2020abjq, 2020pni, 2021dbg, and 2022ffg, in addition to SN 2023ixf and comparison-sample SNe 2013ab and 2021yja, show consistency with $M_{\rm ZAMS} = 10$–12.5 $M_\odot$ models. Finally, only three objects, all

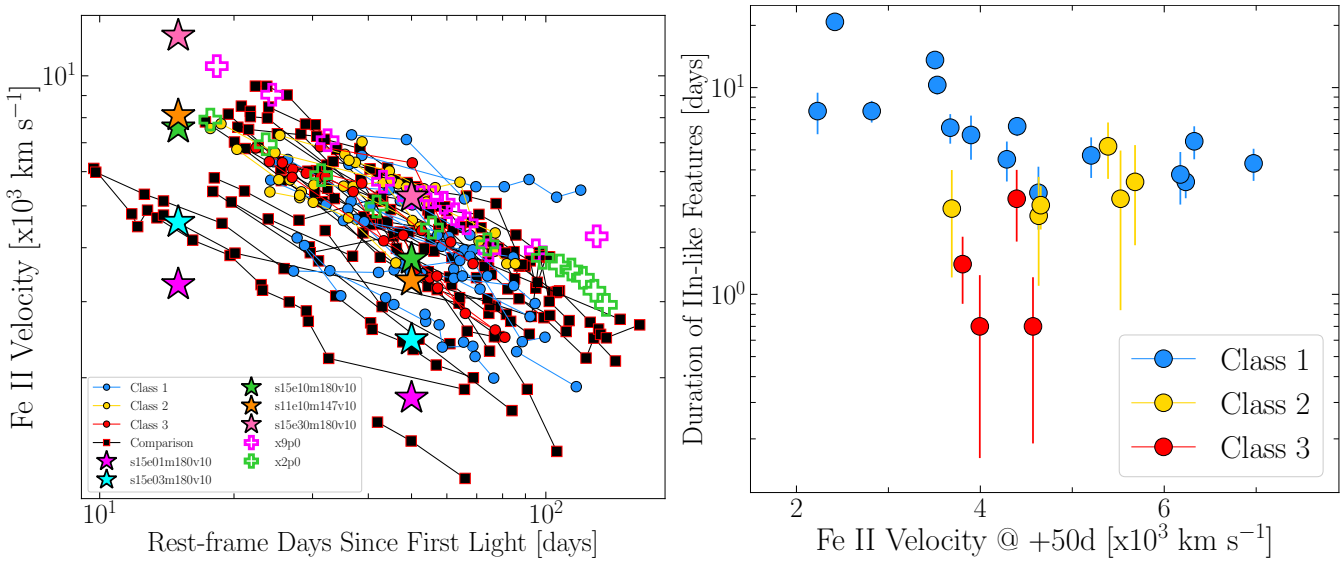

Figure 14. Left: Fe II velocity measurements for gold/silver- (blue, yellow, red circles) and comparison-sample (black squares) objects during and after the plateau light-curve phase. Model predictions with varying explosion energies (0.1–3 B) are shown as stars (L. Dessart et al. 2010) and varying ejecta masses as plus signs (D. J. Hillier & L. Dessart 2019). Higher photospheric velocities in gold/silver-sample objects are likely due to lower ejecta masses than extreme kinetic energies. Right: Measured photospheric Fe II velocities relative to IIn-like feature duration for gold/silver-sample objects. A possible correlation exists where objects with longer $t_{\rm IIn}$ also have lower photospheric velocities, suggesting a link between CSM-interaction timescales and explosion kinetic energy.

in Classes 2 and 3, are consistent with slightly higher masses of 13.5–14.5 $M_\odot$. Intriguingly, we find no SNe II in our sample that are consistent with the high-mass progenitor model using this ZAMS mass estimation metric. Furthermore, we directly compare synthetic model spectra from A. Jerkstrand et al. (2014), A. Jerkstrand et al. (2018), and L. Dessart et al. (2021) with sample data at similar phases after normalizing by the integrated optical luminosity. As shown in Appendix Figures A2–A4, the best-matched $M_{\rm ZAMS}$ models for this smaller sample of objects are consistent with the masses derived from forbidden-line ratios.

3.6. Type II-P SN Scaling Relations

There are well-established scalings that relate the SN II plateau luminosity at +50 days to progenitor/explosion properties (e.g., ejecta mass, kinetic energy, and progenitor radius), which have also been explored extensively with various stellar evolutionary codes (D. Kasen et al. 2006; D. Kasen & S. E. Woosley 2009; L. Dessart et al. 2013; J. A. Goldberg et al. 2019). Overall, increasing L_{50} requires decreasing ejecta mass, increasing kinetic energy, and/or increasing progenitor radius (e.g., see Equation (22) in J. A. Goldberg et al. 2019). As discussed in Section 3.1, the plateau luminosities of SNe II with IIn-like features are significantly larger than those of the comparison-sample objects, suggesting a variation in the above progenitor/explosion properties. We show in Section 3.2 that some gold/silver-sample events may have low ejecta masses, which could explain the enhanced L_{50} values for those objects specifically. However, if the remaining objects have typical $M_{\rm ej}$, then it is possible that kinetic energy and/or progenitor radius play a role.

While a true estimate of $E_{\rm k}$ is challenging for SNe II, we can gain some insight by examining the evolution of the photospheric velocities measured throughout the plateau phase. As shown in Figure 14, the spread in Fe II velocities at 50 days is similar across both gold/silver and comparison samples. We then compare the velocity measurements to model predictions for varying explosion energies (0.1–3 B) from L. Dessart et al. (2010) and ejecta masses from D. J. Hillier & L. Dessart (2019). While an extreme kinetic energy of 3 B is needed to match the fastest velocities measured at +50 d, lowering the ejecta mass in a standard SN II explosion model can produce a similar effect, suggesting that increased $E_{\rm k}$ is unlikely to be the main factor causing enhanced L_{50} in SNe II with IIn-like signatures. Furthermore, some gold/silver events have $v_{\rm ph} < 3000\,{\rm km\,s^{-1}}$ yet $L_{50} > 3 \times 10^{42}$ erg s^{-1}, suggesting that an additional component is relevant for increasing their plateau luminosity. Therefore, one possibility is that many SNe II with IIn-like signatures arise from RSGs with extended radii (>800 $R_\odot$; B. Davies et al. 2013), which could be related to their enhanced mass loss in the final years before explosion. Alternatively, the plateau luminosity could be boosted by ongoing interaction with more distant, yet still sufficiently dense, CSM (Figure 11). Furthermore, plateau luminosities may be affected by ^{56}Ni mixing in the outer ejecta (e.g., E. Nakar et al. 2016; A. Kozyreva et al. 2019).

We further explore the ambiguity of inferring progenitor properties for CSM-interacting SNe II by applying the relation derived by B. L. Barker et al. (2022) that relates L_{50} and Fe core mass. As shown in Figure 15, the use of plateau brightness, especially for SNe II with IIn-like features, yields Fe core-mass estimates that are only consistent with extremely massive progenitor stars (>25 $M_\odot$) as well as the largest neutron stars in the Universe. While these estimates are not only nonphysical, they are also invalidated by other progenitor mass probes, such as ^{56}Ni mass, nebular emission, and/or plateau duration. Consequently, we strongly caution the use of relationships derived from simulations that relate core and envelope properties given that applications of these relations typically only rely on photometric information and/or do not consider that a significant fraction of SNe II with early-time CSM interaction could be mistaken as standardizable SNe II.

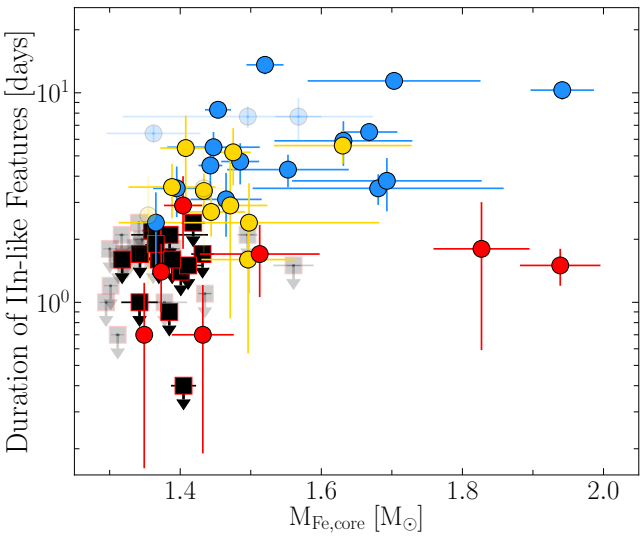

Figure 15. Iron-core mass estimated from L_{50} using the analytic relation derived by B. L. Barker et al. (2022) for gold/silver- (blue, yellow, red circles) and comparison-sample (black squares) objects vs. the IIn-like feature duration. The incredibly large $M_{Fe,core}$ masses inferred for many gold/silver-sample objects demonstrates that this relation is *not* physical—high plateau luminosities are much more likely the result of larger progenitor radii and/or smaller M_{ej} rather than extremely massive progenitor stars ($M_{ZAMS} > 25\,M_\odot$).

4. Discussion

4.1. Connecting Properties of the CSM, Progenitor, and Explosion

A fundamental question in the study of SNe II is how the RSG progenitors of objects with IIn-like features differ from those without this early-time phenomenon. Ideally, we would like to know if there is any correlation between RSG ZAMS (or He core) mass and the creation of confined, high-density CSM capable of producing IIn-like features in some SNe II. As discussed in Section 3.6, the enhanced plateau luminosities of many gold/silver-sample events are consistent with larger progenitor radii and/or low ejecta masses, both of which connect to significant late-stage mass loss. However, among gold/silver-sample SNe, there is a large spread (e.g., 0.01–0.2 $M_\odot$) in the estimated ^{56}Ni masses, which covers model predictions for $M_{ZAMS} = 9.5$–$25\,M_\odot$. Finally, gold/silver-sample objects are unlikely to be highly energetic explosions (e.g., Section 3.6), with some SNe displaying quite slow expansion velocities during and after the plateau (e.g., $v_{ph} < 3000\,km\,s^{-1}$). As shown by simulations in L. Dessart & W. V. Jacobson-Galán (2023), these velocities are not the result of significant ejecta deceleration from early-time CSM interaction because the CDS masses are not large enough. Consequently, these velocities are the result of intrinsically low explosion energies. As shown in the left panel of Figure 14, this has interesting implications for the survival time of IIn-like features because t_{IIn} can be increased for the same CSM density profile if the shock speed is smaller than average (e.g., $<10^4\,km\,s^{-1}$).

To visualize a potential link between progenitor mass and confined CSM properties, we plot the mass-loss rate and CSM density at 10^{14} cm derived from early-time spectroscopic and photometric modeling in WJG24a with respect to the ZAMS mass derived from matching observed nebular spectra to models from L. Dessart et al. (2021). We estimate the range of best-matched ZAMS masses for a given object based on the closest forbidden-line ratio (e.g., Figure 13) at all available spectral epochs, as well as the most consistent model to the complete optical nebular spectrum (e.g., Figure A2). As shown in Figure 16, mass-loss rates and CSM densities range from 10^{-6}–$10^{-1}\,M_\odot\ yr^{-1}$ and 10^{-16}–$10^{-11}\ g\,cm^{-3}$, respectively, for M_{ZAMS} estimates of 9–12 $M_\odot$. For this subsample, we find only one comparison-sample object, SN 2021yja, that has a higher estimated ZAMS mass above 12 $M_\odot$ in addition to six gold/silver-sample objects, as well as SN 2023ixf (shown for reference). Furthermore, it is intriguing that there is a visible scarcity of higher mass ($>12\,M_\odot$) progenitors with low CSM densities at 10^{14} cm. However, we caution that this inference is made for a small sample of only 22 events with both early-time CSM estimates and nebular spectroscopy, which is far from a complete sample (i.e., not controlled). Nevertheless, it motivates the continuous monitoring of SNe II in volume-limited surveys where there are robust constraints on the presence of dense, confined CSM.

Examining potential diversity in SN II progenitor masses in the context of mass-loss mechanisms can directly inform the theoretical picture for the creation of CSM around RSGs. One proposed model for explaining the range of CSM properties is that of convection-driven mass loss ("boil off"), which creates a chromosphere or effervescent zone of static, high-density material at $<5\,R_\star$ (L. Dessart et al. 2017; N. Soker 2021; J. Fuller & D. Tsuna 2024). As shown by the modeling of J. Fuller & D. Tsuna (2024), high-density material, capable of producing early-time IIn-like spectral features, can be created within the immediate vicinity of the RSG during the final years before explosion. Furthermore, while this mechanism is viewed as being stochastic, the amount of material present in this chromosphere is dependent on the convective velocity and, consequently, the mass of the RSG. Therefore, it may be the case that larger RSGs create higher density confined CSM and could then represent the progenitor systems of some SNe II with IIn-like features at early times. Intriguingly, this could explain the general trend seen in Figure 16 between M_{ZAMS} and CSM density, but notably it cannot explain gold/silver-sample SNe with both large CSM densities and smaller inferred progenitor masses (e.g., SNe 2018zd, 2020tlf, and 2021aaqn).

For outlier events with high $\dot{M}$ but low ZAMS mass, an additional mass-loss mechanism needs to be invoked. We now know that wave-driven mass loss is insufficient to produce the CSM densities needed to explain SNe II with IIn-like signatures (e.g., J. Fuller 2017; S. Wu & J. Fuller 2021), but other core processes such as Si deflagrations leading to pre-SN outbursts could be invoked to explain the creation of this dense, confined material (S. E. Woosley & A. Heger 2015). Notably, these core instabilities are specifically predicted for low-mass stars (9–11 $M_\odot$), consistent with the ZAMS mass estimates of SNe 2018zd, 2020tlf, and 2021aaqn. However, more modeling needs to be done in order to properly treat the deflagration in the O core and the consequent injection of energy into the convective RSG envelope (e.g., B. T. H. Tsang et al. 2022). Beyond this, another possibility is binary interaction that leads to the formation of confined, high-density CSM in the final years before explosion. This has been explored for SN II progenitors by A. Ercolino et al. (2024) wherein they model the Case C mass transfer involving an RSG with a main-sequence companion. These simulations show that mass-transfer rates up to $0.01\,M_\odot\ yr^{-1}$ can occur

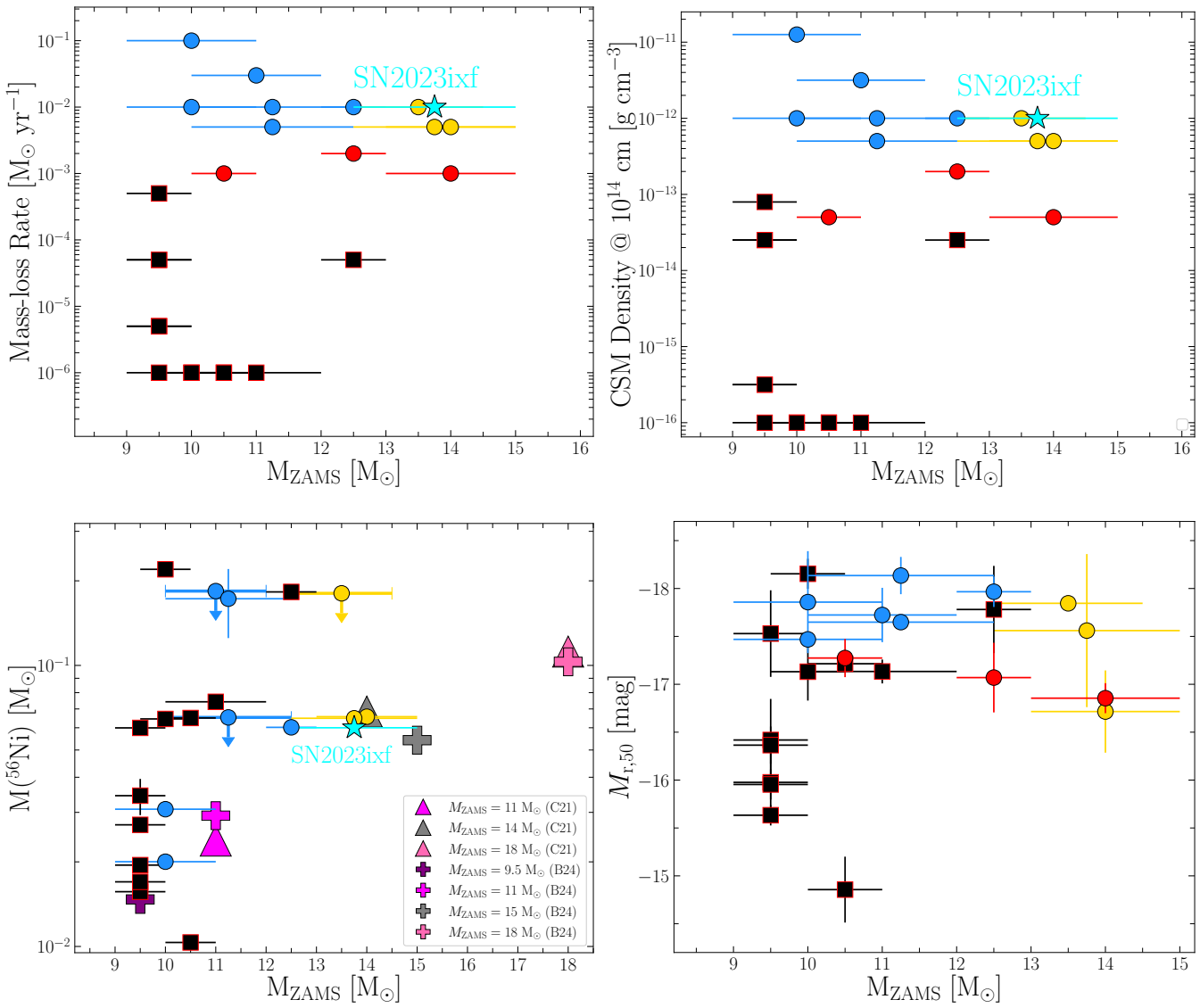

Figure 16. Upper panel: Mass-loss rate and CSM density at 10^{14} cm estimated from early-time spectra (WJG24a) compared to progenitor ZAMS masses inferred from nebular spectra (Section 3.5) for gold/silver (blue, yellow, red circles) and comparison-sample (black squares) objects. SN 2023ixf is shown as a cyan star for reference. Lower panel: ^{56}Ni mass and $M_{r,50}$ values compared to ZAMS masses estimated from nebular spectra. The ^{56}Ni mass predictions for different massive star core-collapse simulations from S. Curtis et al. (2021) and A. Burrows et al. (2024) are shown as triangles and plus signs, respectively.

during late-stage evolution, leading to CSM density profiles that are compatible with SNe II having IIn-like features. Furthermore, explosion modeling of these systems reveals significant diversity among the light-curve and spectral properties of SNe II (L. Dessart et al. 2024).

4.2. Shock-Power Emergence at Late Times

While it is clear that the progenitors of gold/silver-sample objects undergo enhanced mass loss in their final years to decades, what is the nature of the more distant CSM ($>10^{16}$ cm) that traces pre-explosion mass loss in the final centuries to millennia before explosion? As discussed in Section 3.4, some gold/silver-sample objects show evidence for boxy emission within the H /[O I] complex, which is commonly associated with a radiative reverse shock injecting power into a CDS; the bulk of this mass is formed in the first few days postexplosion as the SN shock sweeps up the densest, most local CSM (R. A. Chevalier & C. Fransson 1994; N. N. Chugai et al. 2007; R. A. Chevalier & C. Fransson 2017; L. Dessart et al. 2017; L. Dessart & D. J. Hillier 2022). Notably, the kinetic shock power scales with the mass-loss rate as $L_{\rm sh} = \dot{M} v_{\rm sh}^3 / 2 v_{\rm w}$ and any luminosity from free–free emission of the cooling reverse-shocked gas goes as $L_{\rm RS} \propto (\dot{M}/v_{\rm w})^2$. Therefore, the detection of broad, boxy H emission from the CDS in late-time gold/silver-sample object spectra confirms ongoing CSM interaction with sufficiently dense CSM and larger mass-loss rate (e.g., $>10^{-6} M_\odot$ yr^{-1}) at radii $>10^{16}$ cm (L. Dessart et al. 2023). Furthermore, it has been shown that the range in H widths follows the range in CDS velocity, which scales with total CDS mass and the strength of the CSM interaction (e.g., see L. Dessart & W. V. Jacobson-Galán 2023).

Interestingly, the boxy emission observed in some SNe II is not present in comparison-sample objects until phases >800 days (e.g., SNe 2017eaw, 2021yja; Figure 12) and has been modeled as the emergence of shock power as the primary luminosity source in SNe II at very late times when radioactive-decay power becomes subdominant (L. Dessart

et al. 2023). These observations have interesting implications for late-stage RSG mass loss because if the evolution of these SNe II without IIn-like signatures can be modeled with $\dot{M} \lesssim 10^{-6}\,M_{\odot}\ \mathrm{yr}^{-1}$, then the fact that CDS emission is visible in SNe II with IIn-like signatures as early as 200–300 days implies $\dot{M} > 10^{-6}\,M_{\odot}\ \mathrm{yr}^{-1}$ at a few hundred years before explosion. Furthermore, as demonstrated in Figure 11, there are gold/silver-sample events that either show very weak or no forbidden emission lines, only displaying strong H emission as early as 120 days after first light. These spectra are consistent with models from L. Dessart & D. J. Hillier (2022) with shock powers of 10^{42}–10^{43} erg s^{-1}, suggesting even higher mass-loss rates of $>10^{-5}\,M_{\odot}\ \mathrm{yr}^{-1}$. This spectral morphology/evolution has been discussed in the context of late-time CSM interaction for gold-sample object PTF11iqb by N. Smith et al. (2015), which, like these other SNe, resembles SN II 1998S whose multiwavelength late-time emission suggested a mass-loss rate of $>10^{-4}\,M_{\odot}\ \mathrm{yr}^{-1}$ (D. Pooley et al. 2002; J. Mauerhan & N. Smith 2012; L. Dessart et al. 2016). For such objects, the continuous collision of SN ejecta with intervening CSM is necessary to power CDS emission lines. Narrow P-Cygni profiles from the preshock gas ahead of the shock are not expected to be detectable at such late phases given the decreasing CSM densities and the predicted emissivities of such spectral features compared to CDS emission (L. Dessart et al. 2016).

For SNe II that exhibit strong CSM-interaction signatures within their first hundreds of days, the formation of dust in their CDS may significantly affect the line profiles arising from the dense shell as well as quench forbidden-line luminosity (C. Gall et al. 2014; J. E. Andrews et al. 2016; A. Bevan et al. 2019). As shown in Figure 12, there is a noticeable blue/red asymmetry in the H profile for some of these events, suggesting that dust formation may be present in the CDS. Importantly, dust formed in the CDS will absorb emission arising from the innermost, metal-rich ejecta, and therefore any measurement of forbidden-line flux (e.g., [O I]) will be underestimated (L. Dessart et al. 2025). This phenomenon may be contributing to the lack of forbidden-line emission in some of these gold/silver-sample events at >1 yr postexplosion, but it could also influence the nebular emission-line strength of SNe II that display a blend of expected forbidden lines and a boxy H profile. As shown in SN 2023ixf, the H emission at only $t = 364$ days is strongly affected by dust attenuation, which may be blocking forbidden-line emission from the innermost ejecta. This has significant implications for using the [O I] luminosity as a proxy for progenitor ZAMS mass in SNe with CDS emission. Nevertheless, using forbidden-line ratios of [O I] and [Ca II] to derive ZAMS masses is safe from this effect because both lines will be reduced approximately equally by dust attenuation (L. Dessart et al. 2025).

5. Conclusions

In this paper, we present additional analysis and late-time observations of a sample of SNe II with ("gold/silver") and without ("comparison") spectroscopic evidence for CSM interaction at very early-time phases ($t < 1$ week), originally presented by WJG24a. Below, we summarize the primary observational findings from this work.

1. We compile multiband and pseudobolometric light curves of all gold/silver- and comparison-sample objects with photometry extending beyond $t = 50$ days (Section 3.1). We measure significantly brighter plateau luminosities (L_{50}) and faster decline rates (S_{50}) at $t = 50$ days for gold/silver-sample objects relative to comparison-sample objects. This statistically significant contrast in sample populations is also present in g- and r-band light-curve measurements. However, we find no statistical evidence that the plateau durations of gold/silver- and comparison-sample objects come from separate distributions.
2. We derive ^{56}Ni masses and γ-ray trapping timescales (t_{γ}) by fitting postplateau pseudobolometric light curves with a analytic formalism for the radioactive-decay decline rate observed in SN 1987A (Section 3.2). Similar to previous SN II studies, we observe a general trend between L_{50} and $M(^{56}\mathrm{Ni})$, but with significant variance among gold/silver-sample objects (e.g., some events have relatively low ^{56}Ni mass but large plateau luminosities). We find no statistically significant difference between the $M(^{56}\mathrm{Ni})$ values derived for gold/silver versus comparison samples. Furthermore, we find evidence for incomplete γ-ray trapping ($t_{\gamma} < 250$ days) in five gold/silver- and three comparison-sample objects, implying low ejecta masses of 4–6 $M_{\odot}$ for these SNe.
3. In Section 3.4, we analyze the nebular spectra of 19 gold/silver- and 13 comparison-sample objects at phases $t > 200$ days. We observe a continuum of late-time spectral properties, in particular within the H /[O I] complex. For example, all comparison and five gold/silver SNe show expected forbidden transitions, while the remaining gold/silver-sample objects show "boxy" H emission, either blended with [O I] or as the dominant emission line in the late-time spectrum. This emission is commonly associated with a CDS located between the forward and reverse shocks, containing mostly material swept up in the first few days postexplosion, and powered by ongoing ejecta interaction with significantly dense, distant ($r > 10^{16}$ cm) CSM. Compared to CMFGEN models for late-time shock power from CSM interaction in SNe II by L. Dessart & D. J. Hillier (2022), the boxy H luminosities and emergence times suggest mass-loss rates as high as $10^{-4}\,M_{\odot}\ \mathrm{yr}^{-1}$ at distances $>10^{16}$ cm (i.e., hundreds of years pre-explosion) in some fraction of SN II progenitors.
4. In Section 3.5, we use the nebular SN II models from L. Dessart et al. (2021) to estimate progenitor-star ZAMS masses using both [O I]/[Ca II] line ratios as well as direct spectral comparison for objects with $M(^{56}\mathrm{Ni})$ measurements that can be used for normalization. Intriguingly, we find that most sample objects with nebular spectra can be matched by models for M_{ZAMS} 9–11 $M_{\odot}$, while only 7 SNe II are best described by models with $M_{\mathrm{ZAMS}} \geqslant 12.5\,M_{\odot}$. However, we find no sample objects consistent with progenitor masses $>15\,M_{\odot}$.
5. Placing the plateau properties of gold/silver-sample objects in the context of SN II scaling relations indicates that the large L_{50} values may be related to either lower ejecta masses and/or higher kinetic energies and/or large progenitor radii. The photospheric velocities of

SNe II with IIn-like features confirm that they do not arise from intrinsically energetic explosions and suggest that either lower ejecta mass and/or envelope inflation is a primary cause of their large plateau luminosities. However, we note that significantly strong, ongoing CSM interaction may contribute to the brightness of some objects. Furthermore, we show that SN II observables such as L_{50} are highly inaccurate metrics for progenitor core properties (e.g., Fe core mass).

6. We compare the mass-loss rates and CSM densities at 10^{14} cm derived from early-time observations (e.g., WJG24a) to the ZAMS masses inferred from nebular spectra in Figure 16. SNe II with mass-loss rates ranging from 10^{-6} to $10^{-1}\,M_{\odot}\ \mathrm{yr}^{-1}$ ($\rho_{14} = 10^{-16}$–$10^{-11}\ \mathrm{g\,cm}^{-3}$) can all be described by low-mass progenitor models (e.g., 9–11 $M_{\odot}$), while only SNe II consistent with $M_{\mathrm{ZAMS}} > 12\,M_{\odot}$ models have CSM densities at the upper end of the continuum. If representative of all SN II progenitors, it suggests multiple channels for enhanced mass loss in the final years before explosion: one that may be progenitor-mass dependent (e.g., convection-driven) and one that is more stochastic (e.g., eruptions, binary interaction).

This study highlights the need for continuous, multi-wavelength monitoring of SNe II throughout their evolution. Furthermore, it is necessary to include knowledge gleamed from early-time observations (e.g., confined CSM densities) when analyzing large samples of SNe II during their plateau and at late times. Obtaining larger spectroscopically and volumetrically complete samples of SNe II with late-time light curves and nebular spectra is essential to better constrain the progenitors of all SNe II, in particular those with large CSM densities at radii $<10^{15}$ cm.

6. Acknowledgments

We thank Jared Goldberg and Jim Fuller for valuable discussions.

The Young Supernova Experiment (YSE) and its research infrastructure are supported by the European Research Council under the European Union's Horizon 2020 research and innovation program (ERC grant Agreement No. 101002652, PI K. Mandel), the Heising-Simons Foundation (2018-0913, PI R. Foley; 2018-0911, PI R. Margutti), NASA (NNG17PX03C, PI R. Foley), NSF (AST-1720756, AST-1815935, PI R. Foley), the David & Lucille Packard Foundation (PI R. Foley), VILLUM FONDEN (project #16599, PI J. Hjorth), and the Center for AstroPhysical Surveys (CAPS) at NCSA and the University of Illinois Urbana-Champaign.

W.J.-G. is supported by NASA through Hubble Fellowship grant HSTHF2-51558.001-A awarded by the Space Telescope Science Institute, which is operated for NASA by the Association of Universities for Research in Astronomy, Inc., under contract NAS5-26555. This research was supported in part by the NSF under grant PHY-1748958. The Margutti team at UC Berkeley is partially funded by the Heising-Simons Foundation under grants #2018-0911 and #2021-3248 (PI R. Margutti). R.C. acknowledges support from NASA Swift grant 80NSSC22K0946. The TReX team at UC Berkeley is supported in part by the NSF under grants AST-2221789 and AST-2224255, and by the Heising-Simons Foundation under grant #2021-3248 (PI R. Margutti).

C.D.K. gratefully acknowledges support from the NSF through AST-2432037, the HST Guest Observer Program through HST-SNAP-17070 and HST-GO-17706, and from JWST Archival Research through JWST-AR-6241 and JWST-AR-5441. C.G. and D.F are supported by a VILLUM FONDEN Young Investigator Grant (project #25501) and VILLUM FONDEN Experiment grant (VIL69896). This work was funded by ANID, Millennium Science Initiative, ICN12_009. The work of X.W. is supported by the National Natural Science Foundation of China (NSFC grants 12288102 and 12033003) and the New Cornerstone Science Foundation through the XPLORER PRIZE. This work was granted access to the HPC resources of TGCC under the allocation 2021–A0110410554 and 2022–A0130410554 made by GENCI, France. This research was supported by the Munich Institute for Astro-, Particle and BioPhysics (MIAPbP) which is funded by the Deutsche Forschungsgemeinschaft (DFG, German Research Foundation) under Germany's Excellence Strategy —EXC-2094–390783311. K.A.B. is supported by an LSSTC Catalyst Fellowship; this publication was thus made possible through the support of grant 62192 from the John Templeton Foundation to LSSTC. The opinions expressed in this publication are those of the authors and do not necessarily reflect the views of LSSTC or the John Templeton Foundation.

A.V.F.'s research group at UC Berkeley acknowledges financial assistance from the Christopher R. Redlich Fund, as well as donations from Gary and Cynthia Bengier, Clark and Sharon Winslow, Alan Eustace and Kathy Kwan, William Draper, Timothy and Melissa Draper, Briggs and Kathleen Wood, and Sanford Robertson (W.Z. is a Bengier-Winslow-Eustace Specialist in Astronomy, T.G.B. is a Draper-Wood-Robertson Specialist in Astronomy, Y.Y. was a Bengier-Winslow-Robertson Fellow in Astronomy). Numerous other donors to his group and/or research at Lick Observatory include Douglas and Judith Adams, Raymond Adams, Lawrence Anderson, Charlie Baxter and Jinee Tao, Duncan Beardsley, Eric Behrens and Joyce Hicks, Barbara Berliner, Jack Bertges, Susan Broadston, Ruth Bromer and Joseph Huberman, Ann Brown, Patrick Bukowski and Eve Grossman-Bukowski, Michael and Sharon Burch, Tina Butler, Richard and Susan Cardwell, Alan and Jane Chew, Donna Clarke, Jim Connelly and Anne Mackenzie, Christopher and Patricia Cook, Laurence and Carole Coole, Curtis and Shelley Covey, Roger Cukras, Michael Danylchuk, Lisa Danylchuk, Robert and Margaret Davenport, Byron and Allison Deeter, James and Hilda DeFrisco, Darril dela Torre and Helen Levay, Paul and Margaret Denning, Jane and Patrick Donnelly, Barbara Edwards, Paul and Silvia Edwards, Christopher and Joan Ennis, Arthur and Cindy Folker, Peter and Robin Frazier, Heidi Gerster, Ernest Giachetti, Charles and Gretchen Gooding, Jeffrey Green, Richard and Carol Gregor, Misako and Dennis Griffin, Thomas and Dana Grogan, Judith and Timothy Hachman, Gregory Hirsch, Alan and Gladys Hoefer, Russell and Susan Holdstein, the Hugh Stuart Center Charitable Trust, George Hume, Charles and Patricia Hunt, Stephen and Catherine Imbler, John and Virginia Johnson, Ross Jones and Jane Paul, Michael Kast and Rebecca Lyon, Joel Krajewski, Steven Kusnitz, Max Lacounte, Rudi Lindner, Katherine Lipka, Walter and Karen Loewenstern, Gregory Losito and Veronica Bayduza, Jerri Mariott and Michael Silpa, Herbert Masters III, Bruce Maximov and Susan Albert, Louisa McNatt, Joan and Oliver Mellows, Joseph Meyer and Karyn Chung, Bruce and Judith Moorad, Rand Morimoto and Ana Henderson, Eric and Patty Ng, Edward Oates, Doug and Emilie Ogden, Sandra Otellini,

Angelo Paparella, Ned and Ellin Purdom, Charles Pyle, Richard Reeder, Jonathan and Susan Reiter, Richard Rissel, Paul Robinson, Catherine Rondeau, Ben Samman, Geraldine Sandor, Theodore Sarbin Jr., Laura Sawczuk and Luke Ellis, Stanley and Miriam Schiffman, Tom and Alison Schneider, Richard and Betsey Sesler, Ajay Shah and Lata Krishnan, Lauren and Jerry Shen, Hans Spiller, Richard and Shari Stegman, Justin and Seana Stephens, Ilya Strebulaev and Anna Dvornikova, Charles and Darla Stevens, Christopher Stookey and Sandra Yamashiro, Benjamin Sykes, Marie Teixeira, Eric Tilenius, Eudora and James Ting, David Turner III and Joanne Turner, Andrew Waterman, Kirk and Jacqueline Weaver, Gerald and Virginia Weiss, Janet Westin and Mike McCaw, Byron and Nancy Wood, Richard Wylie, Wen Yang, and others.

M.R.D. acknowledges support from the NSERC through grant RGPIN-2019-06186, the Canada Research Chairs Program, and the Dunlap Institute at the University of Toronto. X.W. acknowledges support by the National Natural Science Foundation of China (NSFC grants 12288102 and 12033003). V.A.V. acknowledges support by the NSF under grant AST-2108676. C.R.A. was supported by grants from VILLUM FONDEN (project #16599 and #25501).

Parts of this research were supported by the Australian Research Council Centre of Excellence for Gravitational Wave Discovery (OzGrav), through project number CE230100016. The UCSC team is supported in part by NASA grant 80NSSC20K0953, NSF grant AST-1815935, the Gordon & Betty Moore Foundation, the Heising-Simons Foundation, and by a fellowship from the David and Lucile Packard Foundation to R.J.F.

This work is based in part on observations made with the Nordic Optical Telescope, owned in collaboration by the University of Turku and Aarhus University, and operated jointly by Aarhus University, the University of Turku and the University of Oslo, representing Denmark, Finland and Norway, the University of Iceland and Stockholm University at the Observatorio del Roque de los Muchachos, La Palma, Spain, of the Instituto de Astrofisica de Canarias. Observations were obtained under program P62-507 (PI C. Angus).

This work includes data obtained with the Swope telescope at Las Campanas Observatory, Chile, as part of the Swope Time Domain Key Project (PI A. Piro; CoIs Coulter, Drout, Phillips, Holoien, French, Cowperthwaite, Burns, Madore, Foley, Kilpatrick, Rojas-Bravo, Dimitriadis, Hsiao). We thank Abdo Campillay, Yilin Kong-Riveros, Piera Soto-King, and Natalie Ulloa for observations on the Swope telescope.

Some of the data presented herein were obtained at the W. M. Keck Observatory, which is operated as a scientific partnership among the California Institute of Technology, the University of California, and NASA. The Observatory was made possible by the generous financial support of the W. M. Keck Foundation. The authors wish to recognize and acknowledge the very significant cultural role and reverence that the summit of Maunakea has always had within the indigenous Hawaiian community. We are most fortunate to have the opportunity to conduct observations from this mountain. A major upgrade of the Kast spectrograph on the Shane 3 m telescope at Lick Observatory, led by Brad Holden, was made possible through generous gifts from the Heising-Simons Foundation, William and Marina Kast, and the University of California Observatories. Research at Lick Observatory is partially supported by a generous gift from Google.

Based in part on observations obtained with the Samuel Oschin 48 inch Telescope at the Palomar Observatory as part of the Zwicky Transient Facility project. ZTF is supported by the NSF under grant AST-1440341 and a collaboration including Caltech, IPAC, the Weizmann Institute for Science, the Oskar Klein Center at Stockholm University, the University of Maryland, the University of Washington, Deutsches Elektronen-Synchrotron and Humboldt University, Los Alamos National Laboratories, the TANGO Consortium of Taiwan, the University of Wisconsin at Milwaukee, and the Lawrence Berkeley National Laboratory. Operations are conducted by the Caltech Optical Observatories (COO), the Infrared Processing and Analysis Center (IPAC), and the University of Washington (UW).

The Pan-STARRS1 Surveys (PS1) and the PS1 public science archive have been made possible through contributions by the Institute for Astronomy, the University of Hawaii, the Pan-STARRS Project Office, the Max Planck Society and its participating institutes, the Max Planck Institute for Astronomy, Heidelberg and the Max Planck Institute for Extraterrestrial Physics, Garching, The Johns Hopkins University, Durham University, the University of Edinburgh, the Queen's University Belfast, the Harvard-Smithsonian Center for Astrophysics, the Las Cumbres Observatory Global Telescope Network Incorporated, the National Central University of Taiwan, STScI, NASA under grant NNX08AR22G issued through the Planetary Science Division of the NASA Science Mission Directorate, NSF grant AST-1238877, the University of Maryland, Eotvos Lorand University (ELTE), the Los Alamos National Laboratory, and the Gordon and Betty Moore Foundation.

This work makes use of observations taken by the Las Cumbres Observatory global telescope network. The Las Cumbres Observatory Group is funded by NSF grants AST-1911225 and AST-1911151. The new SALT data presented here were obtained through Rutgers University program 2022-1-MLT-004 (PI S. Jha). Funding for the Lijiang 2.4 m telescope has been provided by the CAS and the People's Government of Yunnan Province.

Facilities: Swift, PO:1.2m, PS1, Shane (Kast), Nickel, MMT (Binospec), Keck I (LRIS), Keck II (DEIMOS), LCOGT, Gemini: South (GMOS).

Software: IRAF (Tody 1986, Tody 1993), photpipe (A. Rest et al. 2005), DoPhot (P. L. Schechter et al. 1993), HOTPANTS (A. Becker 2015), YSE-PZ (D. A. Coulter et al. 2022, 2023), `CMFGEN` (D. J. Hillier & L. Dessart 2012; L. Dessart et al. 2015), `HERACLES` (M. González et al. 2007; N. M. H. Vaytet et al. 2011; L. Dessart et al. 2015), HEAsoft (v6.33; HEASARC 2014), DRAGONS (K. Labrie et al. 2023), Lpipe (D. A. Perley 2019).

Appendix
Supplementary Figures and Tables

Here, we present previously unpublished nebular spectra for the gold/silver-sample objects in Table A1. Light-curve properties for gold/silver- and comparison-sample objects are given in Tables A2–A3. In Figure A1, we display host-galaxy reddening compared to plateau luminosity at $t = 50$ days and the estimated ^{56}Ni mass for gold/silver- and comparison-sample objects. Figures A2 and A4 display best-matched nebular SN II model spectra from A. Jerkstrand et al. (2014), A. Jerkstrand et al. (2018), and L. Dessart et al. (2021) for all gold/silver- and comparison-sample objects with constrained ^{56}Ni mass measurements.

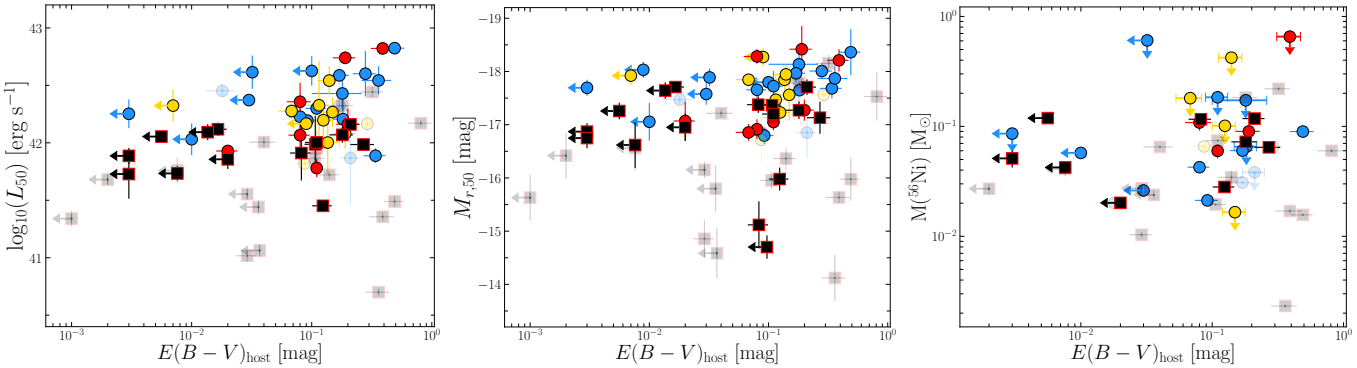

Figure A1. Host-galaxy reddening for gold/silver- and comparison-sample objects compared to measured bolometric and *r*-band luminosities at +50 days as well as ^{56}Ni mass.

Table A1
Optical/Near-IR Spectroscopy

SN Name	UT Date	MJD	Phase[a] (days)	Telescope	Instrument	Wavelength Range (Å)	Data Source
2020abjq	2021-10-16T05:29:32	59503.2	319.8	Gemini	GMOS-S	5178–9885	YSE
2020abjq	2021-11-06T02:42:49	59857.1	340.7	Keck	LRIS	3162–10146	YSE
2020pni	2021-06-12T09:21:36	59377.4	331.6	Keck	DEIMOS	4018–9267	TReX[b]
2021yja	2022-09-22T13:31:10	59844.6	380.2	Keck	LRIS	3136–10192	YSE
2021yja	2023-11-17T12:00:00	60265.5	801.1	Keck	LRIS	5601–10250	TReX
2021dbg	2021-11-06T07:00:00	59524.3	267.2	Keck	LRIS	3162–10147	YSE
2021dbg	2022-01-31T07:12:00	59610.3	353.2	Keck	LRIS	3152–10276	Filippenko
2021aaqn	2022-09-22T13:16:19	59844.6	351.8	Keck	LRIS	3135–10195	YSE
2022ibv	2022-12-11T02:00:00	59924.1	233.6	Gemini	GMOS-S	5201–9885	YSE
2022dml	2022-09-25T05:48:29	59847.2	213.2	Keck	LRIS	3041–10283	TReX
2022ffg	2022-10-31T15:05:46	59883.6	219.8	Keck	LRIS	3040–10327	TReX
2022ffg	2023-02-28T02:00:00	60003.1	339.3	Gemini	GMOS-S	5251–9885	YSE
2022ffg	2023-11-11T12:00:00	60259.5	595.7	Keck	LRIS	5601–10199	TReX
2022jox	2023-02-28T02:00:00	60003.1	339.3	Gemini	GMOS-S	5701–9887	YSE

Notes.
[a] Relative to first light.
[b] Transient Extragalactic team at UC Berkeley (PIs Margutti and Chornock)

Table A2
Gold/Silver-sample Photometric Properties

Name	$\log_{10}(L_{50})$ (erg s^{-1})		$M_{g,50}$ (mag)		$M_{r,50}$ (mag)		$S_{\mathrm{UV\ OIR},50}$		$S_{g,50}$		$S_{g,50}$		t_{PT} (days)		$M(^{56}\mathrm{Ni})$ ($M_\odot$)		t_γ (days)	
PTF11iqb[1]	42.25	0.13	…		−17.69	0.15	−1.5e-02	1.8e-03	…		7.4e-03	3.4e-04	120.11	2.14	<8.6e-02		269.5	101.7
2017ahn[1]	41.87	0.40	−16.26	0.43	−16.86	0.43	−1.8e-02	5.6e-03	4.7e-02	6.8e-04	3.0e-02	5.7e-04	60.51	2.22	<3.8e-02		134.9	23.5
2018zd[1]	42.32	0.37	−17.60	0.53	−17.86	0.53	−1.0e-02	5.4e-03	2.0e-02	9.2e-04	9.7e-03	9.2e-04	120.76	6.27	3.1e-02	4.0e-04	481.1	25.2
2019ust[1]	42.60	0.20	−17.63	0.16	−18.01	0.15	−1.1e-02	2.8e-03	3.7e-02	9.0e-04	1.9e-02	2.7e-04	>93.32		…		…	
2019qch[1]	42.63	0.13	−17.57	0.10	−17.80	0.09	−1.1e-02	1.8e-03	1.9e-02	6.8e-04	7.8e-03	2.7e-04	>73.11		…		…	
2020abjq[1]	42.30	0.06	−17.36	0.15	−17.72	0.28	−1.0e-02	8.8e-04	3.5e-02	3.0e-04	1.1e-02	3.5e-03	>71.66		<1.8e-01		202.1	24.9
2020pni[1]	42.21	0.18	−17.19	0.10	−17.65	0.07	−1.2e-02	2.7e-03	2.7e-02	1.4e-03	1.8e-02	7.8e-04	>49.45		<6.5e-02		486.1	229.8
2020tlf[1]	42.45	0.05	−17.26	0.08	−17.47	0.08	−7.5e-03	6.8e-04	2.3e-02	2.1e-04	1.3e-02	2.1e-04	122.66	1.52	2.0e-02	5.8e-04	346.5	59.0
2020abtf[1]	42.19	0.05	−16.44	0.16	−16.80	0.16	−3.7e-03	6.2e-04	1.8e-02	3.5e-04	8.7e-03	2.6e-04	125.00	5.00	2.1e-02	5.4e-04	…	
2020sic[1]	41.89	0.06	…		−17.68	0.19	−2.9e-03	9.5e-04	…		1.0e-02	1.6e-03	…		…		…	
2021aek[1]	42.54	0.12	−17.73	0.25	−17.87	0.23	−1.3e-02	1.7e-03	2.1e-02	2.8e-03	5.4e-03	2.2e-03	>136.03		…		…	
2021afkk[1]	42.22	0.05	−17.12	0.16	−17.65	0.16	−1.7e-02	7.4e-04	3.9e-02	6.0e-04	2.2e-02	5.3e-04	59.83	1.01	4.3e-02	8.5e-04	…	
2021dbg[1]	42.43	0.14	−17.84	0.16	−18.14	0.19	−7.9e-03	2.0e-03	2.2e-02	6.6e-04	7.0e-03	1.7e-03	>144.42		1.7e-01	4.8e-02	…	
2021mqh[1]	42.03	0.14	−16.39	0.23	−17.05	0.35	−1.1e-02	1.8e-03	3.5e-02	2.5e-03	2.0e-02	4.9e-03	>69.70		5.7e-02	4.3e-03	…	
2021tyw[1]	42.37	0.05	−17.52	0.20	−17.58	0.20	−6.8e-03	6.7e-04	9.3e-03	4.6e-04	2.1e-03	5.0e-04	142.00	5.00	2.6e-02	3.4e-03	…	
2021zj[1]	42.61	0.14	−17.48	0.17	−17.89	0.17	−4.6e-03	2.1e-03	2.4e-03	1.2e-03	2.7e-03	1.2e-03	137.38	2.61	<6.1e-01		…	
2021wvd[1]	…		…		…		…		…		…		>42.95		…		…	
2022ffg[1]	42.59	0.05	−17.86	0.15	−17.97	0.16	−1.5e-02	6.4e-04	3.5e-02	1.4e-04	1.9e-02	5.7e-04	>92.88		6.0e-02	9.9e-04	…	
2022pgf[1]	42.82	0.03	−18.14	0.44	−18.36	0.43	−1.6e-02	4.2e-04	4.3e-02	1.2e-03	3.2e-02	2.4e-04	150.00	5.00	9.0e-02	9.4e-03	…	
2022prv[1]	43.30	0.07	−17.86	0.15	−18.03	0.15	−8.1e-03	1.1e-03	2.2e-02	2.4e-04	7.1e-03	3.6e-04	>72.39		…		…	
PTF10gva[2]	42.32	0.14	…		−17.92	0.17	−9.5e-03	2.2e-03	…		2.0e-02	1.2e-03	>49.98		…		…	
PTF10abyy[2]	42.17	0.03	…		−18.27	0.17	−8.6e-03	4.1e-04	…		1.2e-02	6.5e-04	65.02	0.53	…		…	
2014G[2]	42.17	0.09	−16.96	0.80	−17.56	0.80	−1.2e-02	1.2e-03	3.7e-02	8.9e-04	2.3e-02	7.2e-04	84.19	1.93	6.5e-02	4.4e-03	182.2	12.7
2015bf[2]	42.33	0.39	…		−17.47	0.46	−7.6e-03	5.4e-03	…		1.1e-02	6.2e-03	>56.67		…		…	
2016blz[2]	42.08	0.13	…		…		−8.1e-03	1.9e-03	…		…		>149.54		…		…	
2018dfc[2]	42.00	0.27	−17.07	0.19	−17.84	0.18	−1.1e-02	3.8e-03	4.1e-02	1.6e-03	2.3e-02	1.4e-03	>87.44		…		…	
2021can[2]	42.20	0.14	−16.42	0.08	−17.23	0.12	−1.4e-02	2.0e-03	5.2e-02	9.1e-04	2.4e-02	1.4e-03	61.09	1.73	<1.0e-01		177.2	27.9
2021ont[2]	42.54	0.12	−17.58	0.19	−17.95	0.18	−1.0e-02	1.8e-03	4.1e-02	1.6e-03	2.6e-02	1.4e-03	58.95	2.69	<4.2e-01		…	
2021qvr[2]	42.27	0.13	−16.87	0.26	−17.56	0.49	−1.5e-02	1.8e-03	3.7e-02	8.2e-04	2.1e-02	5.9e-03	90.16	2.76	<1.7e-02		…	
2022dml[2]	42.28	0.06	−17.46	0.08	−17.85	0.08	−8.2e-03	8.2e-04	1.9e-02	5.2e-04	7.6e-03	4.8e-04	92.85	1.71	<1.8e-01		203.1	13.1
2022jox[2]	41.82	0.14	−16.40	0.43	−16.72	0.43	−3.8e-03	1.9e-03	1.7e-02	4.6e-04	8.2e-03	4.1e-04	>65.81		6.6e-02	1.2e-03	478.3	40.9
2013fs[3]	41.93	0.04	−16.50	0.38	−17.07	0.36	−5.7e-03	5.3e-04	1.4e-02	2.8e-03	6.6e-03	2.4e-03	84.37	2.34	…		…	
2018fif[3]	41.78	0.08	−16.22	0.16	−17.05	0.15	−5.5e-03	9.4e-04	1.9e-02	4.7e-04	1.1e-02	9.0e-05	115.00	5.00	8.4e-02	2.0e-02	…	
2020lfn[3]	42.36	0.17	−17.67	0.23	−18.28	0.14	−8.9e-03	2.2e-03	3.5e-02	3.1e-03	1.1e-02	1.8e-03	75.24	2.40	1.1e-01	1.7e-02	…	
2020nif[3]	42.74	0.06	−18.68	0.43	−18.42	0.43	−1.0e-02	9.4e-04	2.2e-02	9.2e-04	2.2e-02	9.2e-04	>62.91		9.0e-02	3.1e-03	397.7	40.3
2020xua[3]	42.07	0.10	−16.90	0.16	−16.92	0.19	−4.8e-03	1.4e-03	1.6e-02	8.2e-04	7.8e-03	1.6e-03	>92.91		…		…	
2021aaqn[3]	42.16	0.13	−16.50	0.45	−17.27	0.20	−7.3e-03	2.0e-03	3.5e-02	7.0e-03	1.4e-02	2.1e-03	79.08	7.20	…		…	
2021jtt[3]	42.82	0.04	−18.00	0.26	−18.21	0.21	−1.0e-02	5.9e-04	2.7e-02	2.6e-03	1.6e-02	1.1e-03	>60.44		<6.6e-01		…	
2022ibv[3]	…		−16.24	0.16	−16.85	0.16	…		2.6e-02	5.8e-04	8.1e-03	3.8e-04	>49.62		…		…	

Table A3
Comparison-sample Photometric Properties

Name	$\log_{10}(L_{50})$ (erg s^{-1})		$M_{g,50}$ (mag)		$M_{r,50}$ (mag)		$S_{\rm UV\ OIR,50}$		$S_{g,50}$		$S_{g,50}$		$t_{\rm PT}$ (days)		$M(^{56}{\rm Ni})$ ($M_\odot$)		t_γ (days)	
2013ft	41.06	0.06	...		−14.59	0.48	−3.4e-03	8.3e-04	...		−2.7e-03	2.3e-03	>127.34		...		...	
2013am	41.49	0.05	...		−15.98	0.41	−1.9e-03	6.6e-04	...		1.7e-03	4.2e-04	107.33	2.23	1.6e-02	3.3e-04	...	
2013ab	41.95	0.16	−16.71	0.12	−17.13	0.12	−5.6e-03	2.2e-03	1.2e-02	1.1e-03	7.9e-03	1.3e-03	101.98	1.03	7.4e-02	8.1e-04	...	
2016X	41.68	0.05	−15.80	0.43	−16.42	0.43	−4.7e-03	6.9e-04	2.1e-02	2.2e-04	3.0e-03	2.4e-04	95.42	0.57	2.7e-02	5.1e-04	...	
2016aqf	41.02	0.05	−14.40	0.33	−14.86	0.34	−1.3e-03	7.2e-04	5.8e-03	2.2e-03	7.8e-04	2.5e-03	>127.34		1.0e-02	6.1e-04	312.5	24.6
2017eaw	42.01	0.05	−16.94	0.08	−17.21	0.08	−2.9e-03	6.2e-04	5.0e-03	8.9e-04	5.1e-04	7.9e-04	116.82	0.22	6.5e-02	8.3e-04	408.3	6.0
2017gmr	42.44	0.05	−17.71	0.16	−18.15	0.16	−5.1e-03	6.5e-04	1.8e-02	5.1e-04	4.4e-03	3.6e-04	94.49	0.55	2.2e-01	7.3e-03	253.0	24.8
2018lab	41.36	0.04	−15.11	0.12	−15.63	0.11	−2.9e-03	5.5e-04	1.5e-02	1.6e-03	1.7e-03	1.3e-03	>110.0		1.7e-02	7.6e-04	...	
2018kpo	41.73	0.21	−16.39	0.16	−16.87	0.16	−6.2e-03	3.5e-03	1.1e-02	6.5e-04	3.2e-03	7.5e-04	>63.21		5.1e-02	8.9e-03	346.0	87.6
2018cuf	41.99	0.02	−16.72	0.30	−17.13	0.30	−4.7e-03	2.9e-04	1.2e-02	2.2e-04	4.2e-03	1.7e-04	111.39	0.75	6.5e-02	7.3e-04	...	
2019edo	41.73	0.06	−16.02	0.43	−16.62	0.43	−3.1e-03	8.2e-04	1.0e-02	2.1e-04	3.5e-03	1.8e-04	88.47	1.85	4.2e-02	4.3e-03	373.3	94.5
2019nvm	42.16	0.05	−17.37	0.15	−17.71	0.15	−6.3e-03	6.9e-04	1.5e-02	2.0e-04	9.8e-03	1.4e-04	>91.38		1.2e-01	5.3e-04	...	
2019pjs	41.55	0.05	−15.70	0.17	−16.15	0.16	−2.8e-03	6.4e-04	6.1e-03	9.6e-04	3.5e-03	6.1e-04	>75.40		2.7e-02	1.4e-03	325.9	42.5
2019enr	...		...		...		...		...		...		>32.65		...		...	
2020ekk	41.86	0.08	−16.41	0.22	−16.95	0.26	−6.1e-03	1.1e-03	2.1e-02	2.3e-03	1.1e-02	3.1e-03	105.42	1.21	2.0e-02	1.5e-03	236.8	42.9
2020jfo	41.72	0.03	−15.96	0.20	−16.36	0.19	−7.8e-03	5.1e-04	2.5e-02	2.9e-04	1.3e-02	1.1e-04	66.24	0.36	3.4e-02	5.1e-03	194.9	19.8
2020fqv	42.17	0.03	−16.98	0.45	−17.53	0.45	−3.6e-03	3.6e-04	2.1e-02	5.4e-04	6.0e-03	1.8e-04	113.26	1.10	6.0e-02	2.2e-03	480.2	54.0
2020mjm	41.76	0.11	−16.13	0.43	−16.56	0.43	−3.2e-03	1.5e-03	2.3e-03	2.8e-04	−6.7e-04	2.5e-04	>85.45		4.1e-02	5.9e-03	208.4	20.9
2020dpw	41.44	0.06	−15.06	0.43	−15.80	0.43	−2.9e-03	8.2e-04	1.2e-02	2.9e-04	1.7e-03	1.6e-04	114.07	3.49	2.4e-02	9.9e-05	...	
2020acbm	41.91	0.24	−16.73	0.16	−17.38	0.15	−5.5e-03	3.0e-03	2.0e-02	9.0e-04	9.8e-03	4.8e-04	>78.74		1.2e-01	6.7e-03	...	
2021vaz	42.07	0.07	−16.83	0.15	−17.26	0.16	−5.2e-03	9.6e-04	1.3e-02	3.2e-04	1.0e-02	7.1e-04	104.90	1.20	7.2e-02	2.5e-03	...	
2021ass	41.45	0.04	−15.37	0.37	−15.98	0.22	−3.1e-03	5.6e-04	2.1e-03	5.0e-03	3.2e-03	1.2e-03	>65.45		2.8e-02	2.5e-04	413.5	13.1
2021gmj	41.87	0.01	−15.45	0.16	−15.95	0.16	−2.7e-04	1.2e-04	4.8e-03	3.9e-04	8.8e-04	2.2e-04	111.97	1.94	1.9e-02	3.3e-04	465.5	49.6
2021rhk	...		...		...		...		...		...		>23.93		...		...	
2021uoy	41.99	0.25	−16.63	0.30	−17.37	0.18	−7.3e-03	3.4e-03	2.1e-02	3.6e-03	1.4e-02	1.3e-03	>98.81		...		...	
2021yja	42.32	0.03	−17.48	0.46	−17.78	0.46	−3.8e-03	4.2e-04	9.5e-03	3.8e-04	4.2e-03	2.7e-04	124.65	0.37	1.8e-01	3.0e-03	404.6	15.6
2021adly	...		...		...		...		...		...		>119.80		...		...	
2021apg	41.89	0.07	−15.92	0.17	−16.75	0.19	−1.8e-03	1.0e-03	1.5e-02	1.0e-03	3.8e-03	1.8e-03	106.61	3.61	...		...	
2021gvm	42.12	0.06	−16.70	0.11	−17.71	0.09	−9.1e-03	8.2e-04	3.0e-02	1.1e-03	1.2e-02	4.9e-04	96.04	0.61	...		...	
2021ucg	42.05	0.04	−16.88	0.16	−17.26	0.16	−2.8e-03	6.2e-04	3.6e-03	5.2e-04	2.9e-03	3.4e-04	123.53	1.11	1.2e-01	1.9e-03	...	
2022inn	...		−14.09	0.39	−14.70	0.22	...		8.6e-03	5.8e-03	−2.6e-03	2.9e-03	>48.97		...		...	
2022fuc	41.34	0.07	−15.09	0.43	−15.63	0.43	−4.2e-03	9.8e-04	9.2e-03	6.3e-04	5.2e-03	3.2e-04	107.48	10.26	...		...	
2022jzc	40.70	0.03	−13.46	0.44	−14.12	0.43	−7.8e-04	4.4e-04	4.1e-03	9.1e-04	−5.9e-03	6.9e-04	>59.61		2.3e-03	8.7e-05	...	
2022ovb	42.09	0.07	−16.98	0.16	−17.64	0.15	−3.3e-03	9.3e-04	1.3e-02	3.8e-04	5.9e-03	2.8e-04	101.82	6.35	...		...	
2022frq	42.00	0.04	−16.83	0.18	−17.22	0.16	−2.8e-03	5.3e-04	9.5e-03	1.4e-03	3.4e-04	6.2e-04	120.00	5.00	...		...	

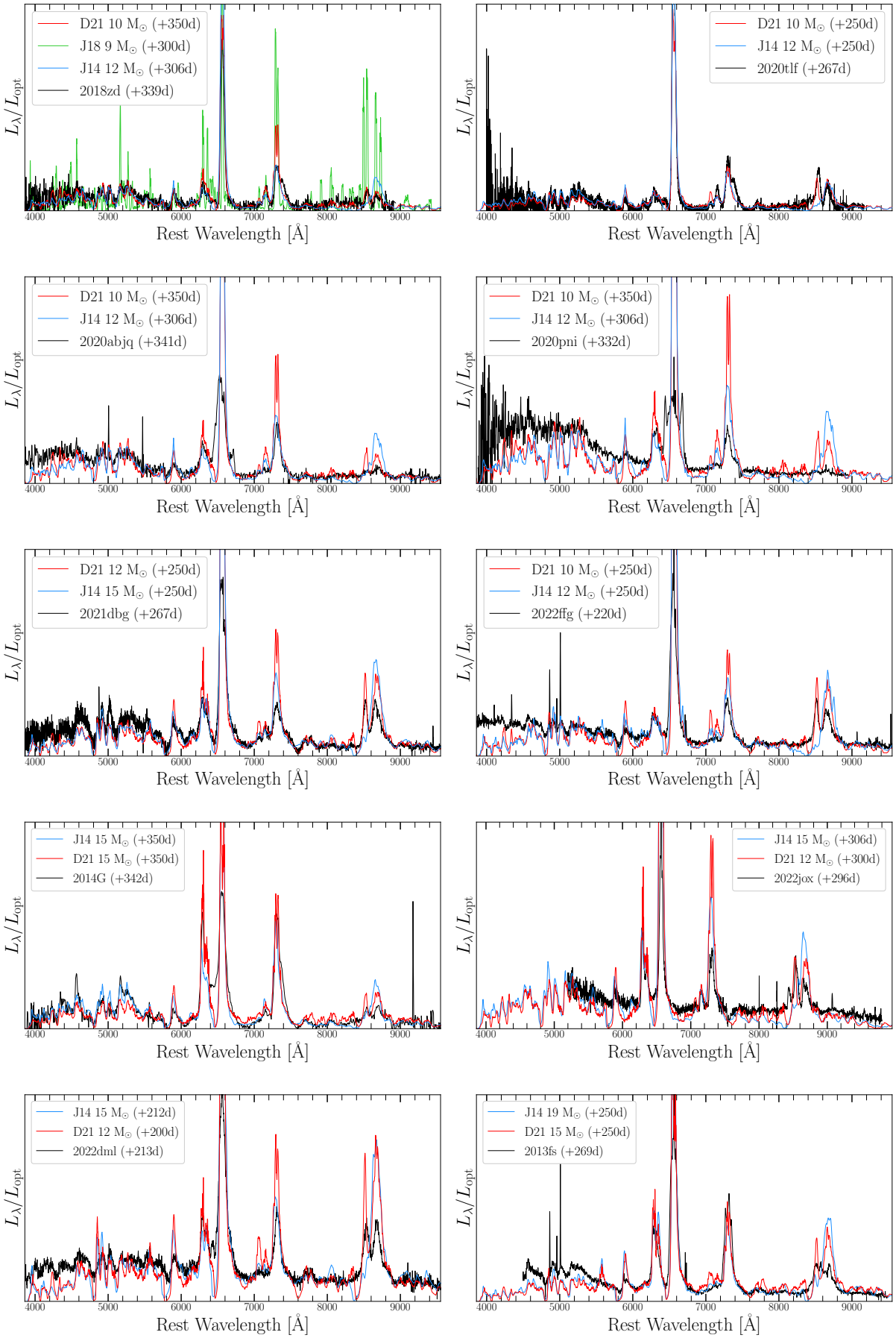

Figure A2. Nebular spectra of sample objects (black) compared to best-matched model spectra from L. Dessart et al. (2021) (red) and A. Jerkstrand et al. (2014) (blue).

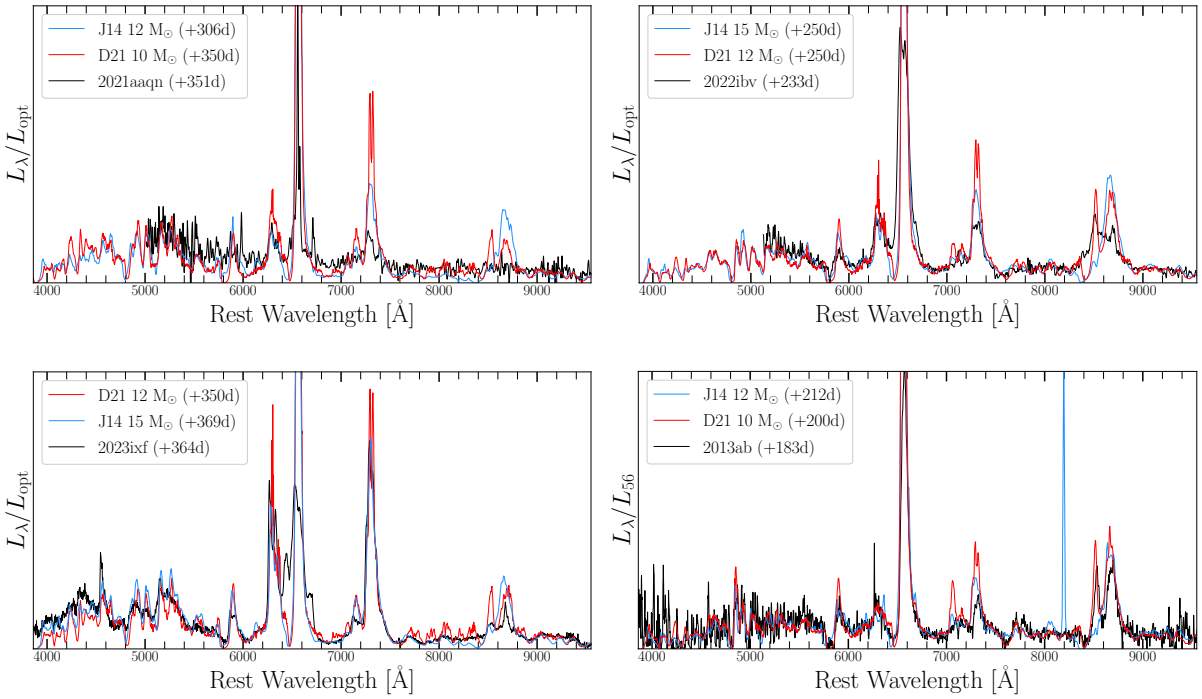

Figure A3. Nebular spectra of sample objects (black) compared to best-matched model spectra from L. Dessart et al. (2021) (red) and A. Jerkstrand et al. (2014) (blue).

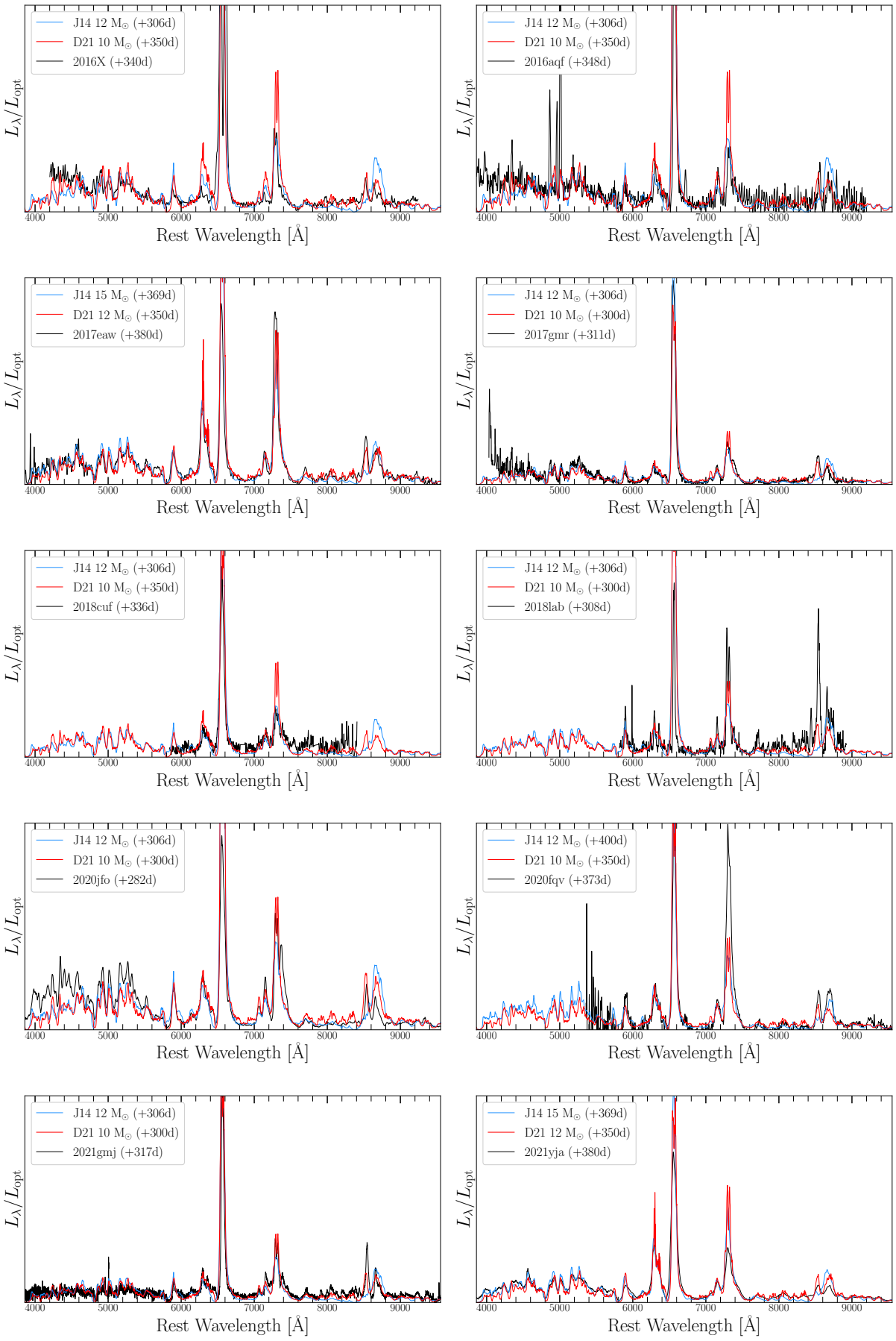

Figure A4. Nebular spectra of sample objects (black) compared to best-matched model spectra from L. Dessart et al. (2021) (red) and A. Jerkstrand et al. (2014) (blue).

ORCID iDs

W. V. Jacobson-Galán https://orcid.org/0000-0002-3934-2644
L. Dessart https://orcid.org/0000-0003-0599-8407
K. W. Davis https://orcid.org/0000-0002-5680-4660
K. A. Bostroem https://orcid.org/0000-0002-4924-444X
C. D. Kilpatrick https://orcid.org/0000-0002-5740-7747
R. Margutti https://orcid.org/0000-0003-4768-7586
A. V. Filippenko https://orcid.org/0000-0003-3460-0103
R. J. Foley https://orcid.org/0000-0002-2445-5275
R. Chornock https://orcid.org/0000-0002-7706-5668
G. Terreran https://orcid.org/0000-0003-0794-5982
D. Hiramatsu https://orcid.org/0000-0002-1125-9187
M. Newsome https://orcid.org/0000-0001-9570-0584
E. Padilla Gonzalez https://orcid.org/0000-0003-0209-9246
C. Pellegrino https://orcid.org/0000-0002-7472-1279
D. A. Howell https://orcid.org/0000-0003-4253-656X
J. P. Anderson https://orcid.org/0000-0003-0227-3451
C. R. Angus https://orcid.org/0000-0002-4269-7999
K. Auchettl https://orcid.org/0000-0002-4449-9152
T. G. Brink https://orcid.org/0000-0001-5955-2502
R. Cartier https://orcid.org/0000-0003-4553-4033
D. A. Coulter https://orcid.org/0000-0003-4263-2228
T. de Boer https://orcid.org/0000-0001-5486-2747
M. R. Drout https://orcid.org/0000-0001-7081-0082
N. Earl https://orcid.org/0000-0003-1714-7415
K. Ertini https://orcid.org/0000-0001-7251-8368
J. R. Farah https://orcid.org/0000-0003-4914-5625
D. Farias https://orcid.org/0000-0002-6886-269X
C. Gall https://orcid.org/0000-0002-8526-3963
H. Gao https://orcid.org/0000-0003-1015-5367
A. Haynie https://orcid.org/0000-0003-4287-4577
G. Hosseinzadeh https://orcid.org/0000-0002-0832-2974
A. L. Ibik https://orcid.org/0000-0003-2405-2967
S. W. Jha https://orcid.org/0000-0001-8738-6011
D. O. Jones https://orcid.org/0000-0002-6230-0151
D. Langeroodi https://orcid.org/0000-0001-5710-8395
N. LeBaron https://orcid.org/0000-0002-2249-0595
E. A. Magnier https://orcid.org/0000-0002-7965-2815
A. L. Piro https://orcid.org/0000-0001-6806-0673
S. I. Raimundo https://orcid.org/0000-0002-6248-398X
A. Rest https://orcid.org/0000-0002-4410-5387
S. Rest https://orcid.org/0000-0002-3825-0553
R. Michael Rich https://orcid.org/0000-0003-0427-8387
C. Rojas-Bravo https://orcid.org/0000-0002-7559-315X
H. Sears https://orcid.org/0000-0001-8023-4912
K. Taggart https://orcid.org/0000-0002-5748-4558
V. A. Villar https://orcid.org/0000-0002-1125-9187
R. J. Wainscoat https://orcid.org/0000-0002-5814-4061
X.-F. Wang https://orcid.org/0000-0002-7334-2357
A. R. Wasserman https://orcid.org/0000-0002-4186-6164
S. Yan https://orcid.org/0009-0004-4256-1209
J. Zhang https://orcid.org/0000-0002-8296-2590
W. Zheng https://orcid.org/0000-0002-2636-6508

References

Anderson, J. P. 2019, A&A, 628, A7
Anderson, J. P., González-Gaitán, S., Hamuy, M., et al. 2014, ApJ, 786, 67
Andrews, J. E., Gallagher, J. S., Clayton, G. C., et al. 2010, ApJ, 715, 541
Andrews, J. E., Krafton, K. M., Clayton, G. C., et al. 2016, MNRAS, 457, 3241
Andrews, J. E., Pearson, J., Hosseinzadeh, G., et al. 2024, ApJ, 965, 85
Arnett, W. D. 1982, ApJ, 253, 785
Barker, B. L., Harris, C. E., Warren, M. L., O'Connor, E. P., & Couch, S. M. 2022, ApJ, 934, 67
Basko, M. 1994, ApJ, 425, 264
Beasor, E. R., Davies, B., Smith, N., et al. 2020, MNRAS, 492, 5994
Beasor, E. R., & Smith, N. 2022, ApJ, 933, 41
Beasor, E. R., Smith, N., & Jencson, J. E. 2025, ApJ, 979, 117
Becker, A., 2015 Astrophysics Source Code Library, ascl:1504.004
Berger, E., Keating, G., Alexander, K., et al. 2023, TNSAN, 131, 1
Bevan, A., Wesson, R., Barlow, M. J., et al. 2019, MNRAS, 485, 5192
Blinnikov, S. I., & Bartunov, O. S. 1993, A&A, 273, 106
Bose, S., Valenti, S., Misra, K., et al. 2015, MNRAS, 450, 2373
Bostroem, K. A., Pearson, J., Shrestha, M., et al. 2023, ApJL, 956, L5
Bruch, R. J., Gal-Yam, A., Schulze, S., et al. 2021, ApJ, 912, 46
Bruch, R. J., Gal-Yam, A., Yaron, O., et al. 2023, ApJ, 952, 119
Burrows, A., & Vartanyan, D. 2021, Natur, 589, 29
Burrows, A., Wang, T., & Vartanyan, D. 2024, ApJL, 964, L16
Cappellaro, E., Mazzali, P. A., Benetti, S., et al. 1997, A&A, 328, 203
Chandra, P., Chevalier, R. A., Maeda, K., Ray, A. K., & Nayana, A. J. 2024, ApJL, 963, L4
Chevalier, R. A., & Fransson, C. 1994, ApJ, 420, 268
Chevalier, R. A., & Fransson, C. 2017, in Handbook of Supernovae, ed. A. W. Alsabti & P. Murdin (Berlin: Springer), 875
Chugai, N. N., Chevalier, R. A., & Utrobin, V. P. 2007, ApJ, 662, 1136
Clocchiatti, A., & Wheeler, J. C. 1997, ApJ, 491, 375
Coulter, D. A., Jones, D. O., McGill, P., et al. 2022, YSE-PZ: An Open-source Target and Observation Management System, v0.3.0, doi:10.5281/zenodo.7278430
Coulter, D. A., Jones, D. O., McGill, P., et al. 2023, PASP, 135, 064501
Curtis, S., Wolfe, N., Fröhlich, C., et al. 2021, ApJ, 921, 143
Davies, B., & Beasor, E. R. 2018, MNRAS, 474, 2116
Davies, B., Kudritzki, R.-P., Plez, B., et al. 2013, ApJ, 767, 3
Dessart, L., & Audit, E. 2019, A&A, 629, A17
Dessart, L., Audit, E., & Hillier, D. J. 2015, MNRAS, 449, 4304
Dessart, L., Gutiérrez, C. P., Ercolino, A., Jin, H., & Langer, N. 2024, A&A, 685, A169
Dessart, L., Gutiérrez, C. P., Kuncarayakti, H., Fox, O. D., & Filippenko, A. V. 2023, A&A, 675, A33
Dessart, L., & Hillier, D. J. 2019, A&A, 625, A9
Dessart, L., & Hillier, D. J. 2022, A&A, 660, L9
Dessart, L., Hillier, D. J., Audit, E., Livne, E., & Waldman, R. 2016, MNRAS, 458, 2094
Dessart, L., Hillier, D. J., & Sarangi, A. 2025, A&A, 698, A293
Dessart, L., Hillier, D. J., Sukhbold, T., Woosley, S. E., & Janka, H. T. 2021, A&A, 652, A64
Dessart, L., Hillier, D. J., Waldman, R., & Livne, E. 2013, MNRAS, 433, 1745
Dessart, L., & Jacobson-Galán, W. V. 2023, A&A, 677, A105
Dessart, L., John Hillier, D., & Audit, E. 2017, A&A, 605, A83
Dessart, L., Livne, E., & Waldman, R. 2010, MNRAS, 408, 827
Dong, Y., Valenti, S., Bostroem, K. A., et al. 2021, ApJ, 906, 56
Eldridge, J. J., Xiao, L., Stanway, E. R., Rodrigues, N., & Guo, N. Y. 2018, PASA, 35, e049
Elmhamdi, A., Chugai, N. N., & Danziger, I. J. 2003, A&A, 404, 1077
Ercolino, A., Jin, H., Langer, N., & Dessart, L. 2024, A&A, 685, A58
Fabricant, D., Fata, R., Epps, H., et al. 2019, PASP, 131, 075004
Fang, Q., Maeda, K., Ye, H., Moriya, T. J., & Matsumoto, T. 2025, ApJ, 978, 35
Fassia, A., Meikle, W. P. S., Chugai, N., et al. 2001, MNRAS, 325, 907
Folatelli, G., Ferrari, L., Ertini, K., Kuncarayakti, H., & Maeda, K. 2025, A&A, 698, A213
Fransson, C., Challis, P. M., Chevalier, R. A., et al. 2005, ApJ, 622, 991
Fuller, J. 2017, MNRAS, 470, 1642
Fuller, J., & Tsuna, D. 2024, OJAp, 7, 47
Gabler, M., Wongwathanarat, A., & Janka, H.-T. 2021, MNRAS, 502, 3264
Gal-Yam, A. 2017, in Handbook of Supernovae, ed. A. W. Alsabti & P. Murdin (Berlin: Springer), 195
Gal-Yam, A., Arcavi, I., Ofek, E. O., et al. 2014, Natur, 509, 471
Gall, C., Hjorth, J., Watson, D., et al. 2014, Natur, 511, 326
Goldberg, J. A., & Bildsten, L. 2020, ApJL, 895, L45
Goldberg, J. A., Bildsten, L., & Paxton, B. 2019, ApJ, 879, 3
González, M., Audit, E., & Huynh, P. 2007, A&A, 464, 429
Grefenstette, B. W., Brightman, M., Earnshaw, H. P., Harrison, F. A., & Margutti, R. 2023, ApJL, 952, L3
Groh, J. H. 2014, A&A, 572, L11
Gutiérrez, C. P., Anderson, J. P., Hamuy, M., et al. 2017a, ApJ, 850, 89

Gutiérrez, C. P., Anderson, J. P., Hamuy, M., et al. 2017b, ApJ, 850, 90
Hamuy, M. 2003, ApJ, 582, 905
Hillier, D. J., & Dessart, L. 2012, MNRAS, 424, 252
Hillier, D. J., & Dessart, L. 2019, A&A, 631, A8
Hiramatsu, D., Howell, D. A., Moriya, T. J., et al. 2021a, ApJ, 913, 55
Hiramatsu, D., Howell, D. A., Van Dyk, S. D., et al. 2021b, NatAs, 5, 903
Horne, K. 1986, PASP, 98, 609
Hosseinzadeh, G., Kilpatrick, C. D., Dong, Y., et al. 2022, ApJ, 935, 31
Huang, F., Wang, X. F., Hosseinzadeh, G., et al. 2018, MNRAS, 475, 3959
Jacobson-Galán, W. V., Davis, K. W., Kilpatrick, C. D., et al. 2024b, ApJ, 972, 177
Jacobson-Galán, W. V., Dessart, L., Davis, K. W., et al. 2024a, ApJ, 970, 189
Jacobson-Galán, W. V., Dessart, L., Jones, D. O., et al. 2022, ApJ, 924, 15
Jacobson-Galán, W. V., Dessart, L., & Kilpatrick, C. D. 2025, arXiv:2508.11747
Jacobson-Galán, W. V., Dessart, L., Margutti, R., et al. 2023, ApJL, 954, L42
Jacobson-Galán, W. V., Margutti, R., Kilpatrick, C. D., et al. 2021, ApJL, 908, L32
Janka, H. T. 2025, arXiv:2502.14836
Jerkstrand, A., Ertl, T., Janka, H. T., et al. 2018, MNRAS, 475, 277
Jerkstrand, A., Smartt, S. J., Fraser, M., et al. 2014, MNRAS, 439, 3694
Jerkstrand, A., Timmes, F. X., Magkotsios, G., et al. 2015, ApJ, 807, 110
Kasen, D., Thomas, R. C., & Nugent, P. 2006, ApJ, 651, 366
Kasen, D., & Woosley, S. E. 2009, ApJ, 703, 2205
Khazov, D., Yaron, O., Gal-Yam, A., et al. 2016, ApJ, 818, 3
Kilpatrick, C. D., Izzo, L., Bentley, R. O., et al. 2023, MNRAS, 524, 2161
Kozyreva, A., Nakar, E., & Waldman, R. 2019, MNRAS, 483, 1211
Kumar, A., Dastidar, R., Maund, J. R., Singleton, A. J., & Sun, N.-C. 2025, MNRAS, 538, 659
Labrie, K., Anderson, K., Cárdenes, R., Simpson, C., & Turner, J. E. H. 2019, in ASP Conf. Ser. 523, Astronomical Data Analysis Software and Systems XXVII, ed. P. J. Teuben, M. W. Pound, B. A. Thomas, E. M Warner et al., 321
Labrie, K., Simpson, C., Cardenes, R., et al. 2023, RNAAS, 7, 214
Laplace, E., Justham, S., Renzo, M., et al. 2021, A&A, 656, A58
Leonard, D. C., Filippenko, A. V., Barth, A. J., & Matheson, T. 2000, ApJ, 536, 239
Li, G., Wang, X., Yang, Y., et al. 2025, arXiv:2504.03856
Lin, H., Wang, X., Zhang, J., et al. 2021, MNRAS, 505, 4890
Martinez, L., Bersten, M. C., Anderson, J. P., et al. 2022a, A&A, 660, A40
Martinez, L., Bersten, M. C., Anderson, J. P., et al. 2022b, A&A, 660, A41
Matsumoto, T., Metzger, B. D., & Goldberg, J. A. 2025, ApJ, 978, 56
Mauerhan, J., & Smith, N. 2012, MNRAS, 424, 2659
Meza-Retamal, N., Dong, Y., Bostroem, K. A., et al. 2024, ApJ, 971, 141
Miller, J. S., & Stone, R. P. S. 1994, The Kast Double Spectrograph LOTRM 66, Univ. California
Müller-Bravo, T. E., Gutiérrez, C. P., Sullivan, M., et al. 2020, MNRAS, 497, 361
Nakar, E., Poznanski, D., & Katz, B. 2016, ApJ, 823, 127
Nayana, A. J., Margutti, R., Wiston, E., et al. 2025, ApJ, 985, 51
Nymark, T. K., Fransson, C., & Kozma, C. 2006, A&A, 449, 171
Oke, J. B., Cohen, J. G., Carr, M., et al. 1995, PASP, 107, 375
Panjkov, S., Auchettl, K., Shappee, B. J., et al. 2024, PASA, 41, e059
Patat, F., Barbon, R., Cappellaro, E., & Turatto, M. 1994, A&A, 282, 731
Pearson, J., Hosseinzadeh, G., Sand, D. J., et al. 2023, ApJ, 945, 107
Pejcha, O., & Prieto, J. L. 2015, ApJ, 806, 225
Perley, D. A. 2019, PASP, 131, 084503
Planck Collaboration, Aghanim, N., Akrami, Y., et al. 2020, A&A, 641, A6
Pooley, D., Lewin, W. H. G., Fox, D. W., et al. 2002, ApJ, 572, 932
Prochaska, J., Hennawi, J., Westfall, K., et al. 2020, JOSS, 5, 2308
Rest, A., Stubbs, C., Becker, A. C., et al. 2005, ApJ, 634, 1103
Sanders, N. E., Soderberg, A. M., Gezari, S., et al. 2015, ApJ, 799, 208
Schechter, P. L., Mateo, M., & Saha, A. 1993, PASP, 105, 1342
Shivvers, I., Groh, J. H., Mauerhan, J. C., et al. 2015, ApJ, 806, 213
Shrestha, M., Bostroem, K. A., Sand, D. J., et al. 2024a, ApJL, 972, L15
Shrestha, M., Pearson, J., Wyatt, S., et al. 2024b, ApJ, 961, 247
Singh, A., Kumar, B., Moriya, T. J., et al. 2019, ApJ, 882, 68
Singh, A., Srivastav, S., Kumar, B., Anupama, G. C., & Sahu, D. K. 2018, MNRAS, 480, 2475
Smartt, S. J. 2009, ARA&A, 47, 63
Smith, N., Mauerhan, J. C., Cenko, S. B., et al. 2015, MNRAS, 449, 1876
Soker, N. 2021, ApJ, 906, 1
Spiro, S., Pastorello, A., Pumo, M. L., et al. 2014, MNRAS, 439, 2873
Sukhbold, T., Ertl, T., Woosley, S. E., Brown, J. M., & Janka, H. T. 2016, ApJ, 821, 38
Suntzeff, N. B., & Bouchet, P. 1990, AJ, 99, 650
Szalai, T., Vinkó, J., Könyves-Tóth, R., et al. 2019, ApJ, 876, 19
Tartaglia, L., Sand, D. J., Groh, J. H., et al. 2021, ApJ, 907, 52
Teja, R. S., Goldberg, J. A., Sahu, D. K., et al. 2024, ApJ, 974, 44
Terreran, G., Jacobson-Galán, W. V., Groh, J. H., et al. 2022, ApJ, 926, 20
Terreran, G., Jerkstrand, A., Benetti, S., et al. 2016, MNRAS, 462, 137
Tinyanont, S., Ridden-Harper, R., Foley, R. J., et al. 2022, MNRAS, 512, 2777
Tomasella, L., Cappellaro, E., Pumo, M. L., et al. 2018, MNRAS, 475, 1937
Tsang, B. T. H., Kasen, D., & Bildsten, L. 2022, ApJ, 936, 28
Valenti, S., Elias-Rosa, N., Taubenberger, S., et al. 2008, ApJL, 673, L155
Valenti, S., Howell, D. A., Stritzinger, M. D., et al. 2016, MNRAS, 459, 3939
Valenti, S., Sand, D., Stritzinger, M., et al. 2015, MNRAS, 448, 2608
Vartanyan, D., Tsang, B. T. H., Kasen, D., et al. 2025, ApJ, 982, 9
Vaytet, N. M. H., Audit, E., Dubroca, B., & Delahaye, F. 2011, JQSRT, 112, 1323
Weil, K. E., Fesen, R. A., Patnaude, D. J., & Milisavljevic, D. 2020, ApJ, 900, 11
Wheeler, J. C., Johnson, V., & Clocchiatti, A. 2015, MNRAS, 450, 1295
Woosley, S. E., & Heger, A. 2015, ApJ, 810, 34
Wu, S., & Fuller, J. 2021, ApJ, 906, 3
Yaron, O., Perley, D. A., Gal-Yam, A., et al. 2017, NatPh, 13, 510
Zhang, J., Dessart, L., Wang, X., et al. 2024, ApJL, 970, L18
Zhang, J., Lin, H., Wang, X., et al. 2023, SciBu, 68, 2548
Zhang, J., Wang, X., József, V., et al. 2020, MNRAS, 498, 84
Zhang, J., Wang, X., Mazzali, P. A., et al. 2014, ApJ, 797, 5
Zimmerman, E. A., Irani, I., Chen, P., et al. 2024, Natur, 627, 759